
Convergence Analysis of Over-parameterized Deep Linear Networks, and the Principal Components Bias

Guy Hacohen

Daphna Weinshall

The School of Computer Science and Engineering
 The Hebrew University of Jerusalem, 91904 Jerusalem, Israel
 {guy.hacohen, daphna}@mail.huji.ac.il

Abstract

Convolutional Neural networks of different architectures seem to learn to classify images in the same order. To understand this phenomenon, we revisit the over-parametrized deep linear network model. Our analysis of this model’s learning dynamics reveals that the convergence rate of its parameters is exponentially faster along directions corresponding to the larger principal components of the data, at a rate governed by the singular values. We term this convergence pattern the *Principal Components bias (PC-bias)*. We show how the *PC-bias* streamlines the order of learning of both linear and non-linear networks, more prominently in earlier stages of learning. We then compare our results to the spectral bias, showing that both biases can be seen independently, and affect the order of learning in different ways. Finally, we discuss how the PC-bias can explain several phenomena, including the benefits of prevalent initialization schemes, how early stopping may be related to PCA, and why deep networks converge more slowly when given random labels.

1. Introduction

Some properties of deep learning, described in a variety of studies, challenge our understanding of machine learning and how it should behave. Among these findings, recent empirical results (Hacohen et al., 2020) show that neural networks of different architectures and capacity learn a similar function throughout the stages of learning. Thus, if datapoints are ordered by the first time (roughly speaking) that each network instance classifies them correctly, then those rankings are highly correlated, irrespective of initial conditions or the network’s architecture. Below we call this effect *Learning Order Constancy (LOC)*. In agreement with earlier results, these observations imply that the same exam-

ples are consistently learned before the others. Currently, the characteristics of such examples remain unclear.

Such results are especially surprising given the fact that neural models are trained by minimizing complex non-convex objective functions. It is hard to rigorously justify why methods based on gradient descent seem so little affected by the initial conditions and other sources of variability, which are introduced into the training of different model instances.

Theoretical analysis of deep neural network models could unveil some of the mystery, but unfortunately models used in real applications are too complex to be analyzed directly. Instead, simpler *elementary* models, which share some basic properties with real-world models, are analyzed in the hope that the results would shed light on the workings of real networks. Possibly the simplest model is the deep linear network (Saxe et al., 2013; 2019), defined by the concatenation of linear operators. While no longer a universal approximator, its training involves the minimization of a non-convex objective function with a multitude of minima. Consequently, its investigation can shed light on some of the questions we are interested in, and in particular the dynamics of learning when gradient descent is used to explore complex geometric landscapes.

In accordance, in order to investigate the LOC effect, we begin by analyzing neural models through the lens of these simple models (Section 2). We first prove that the convergence of the weights of such models is governed by the eigendecomposition of the raw data, under some mild assumptions, in a phenomenon we term *PC-bias*. We then show empirically that this pattern of convergence is indeed observed in deep linear networks, validating the plausibility of our assumptions. We also show that the LOC effect in deep linear network is determined solely by their PC-bias. A similar (weaker) result is shown for the non-linear two-layer ReLU model introduced in (Allen-Zhu et al., 2018).

Next, we extend the study empirically and investigate the relation between the *PC-bias* and the *LOC* effect in general

deep networks (Section 4). We first show that the order by which examples are learned by linear networks is highly correlated with the order induced by prevalent deep CNN models. We then show directly that the learning order of non-linear CNN models is affected by the principal decomposition of the data. Finally, we show that the *LOC* effect diminishes when the networks are given whitened data, with identical singular values, indicating a tight connection between the *PC-bias* and the *LOC* effect.

1.1. Fourier Analysis and Relation to 'Spectral Bias'

The *PC-bias* is governed by the eigendecomposition of the data in the input space. Interestingly, the eigendecomposition of raw images is closely related to the Fourier analysis of images as long as the statistical properties of images are (approximately) translation-invariant (Simoncelli & Olshausen, 2001; Torralba & Oliva, 2003), see Fig. 1.

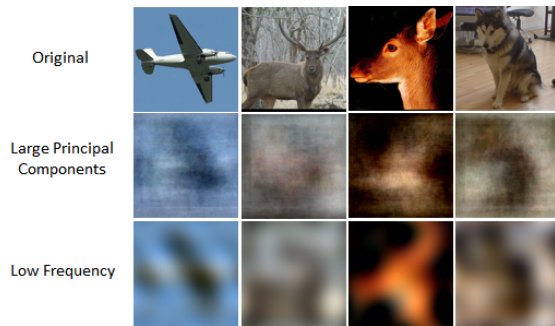


Figure 1. Examples from STL-10, showing the difference between images projected on the largest 20 principal components (middle) and images obtained with a low-pass filter (bottom).

The relation between learning order and the Fourier decomposition of functions in the hypothesis space has been termed *Spectral bias* (Rahaman et al., 2019; Cao et al., 2019). Thus Rahaman et al. (2019) empirically demonstrated that the complexity of classifiers learned by ReLU networks increases with time. Basri et al. (2019; 2020) showed theoretically, by way of analyzing elementary neural network models, that these models first fit the data with low-frequency functions, and gradually add higher frequencies to improve the fit. **Importantly, the Fourier decomposition of classifiers in hypothesis space and PCA decomposition are quite different and often unrelated¹.** Thus *PC-bias* and *spectral bias* are inherently different: the first is guided by spectral properties of the raw data and is additionally blind to class labels, while the second is guided by spectral properties of the learned hypothesis.

In this paper we investigate the relation between these two effects and the *LOC* effect (see Section 5.3), showing that the

¹A low frequency function is fully adequate to classify separable high frequency data.

LOC effect is very robust: (i) if we neutralize the *Spectral bias* by using low complexity models such as deep linear networks, the effect is still observed; (ii) if we neutralize the *PC-bias* by using whitened data, the *LOC* effect persists. Thus the emerging dynamics of learning in general non-linear deep networks is the following: First, while the classifier can still be described by a few low frequencies, the dynamics are controlled by the eigendecomposition of the raw data. As learning proceeds, control of the dynamics slowly shifts to other factors, possibly including the spectral properties of the learned classification function.

1.2. Further Implications

This set of results has interesting implications, as discussed in Section 6, and summarized next. Note that eigendecomposition is blind to class identity. This implies that for a given point distribution and regardless of label distribution, the pattern of convergence is the same, although the error being propagated is clearly different.

Early stopping. It is often observed that when training deep networks with real data, the best generalization accuracy is obtained before convergence. Consequently, early stopping is often prescribed to improve generalization. Our results show that when training deep linear networks, early stopping is beneficial if the eigenvectors corresponding to smaller singular values represent noise. This assumption underlies dimensionality reduction with PCA, and in that sense, early stopping is related to PCA. In Section 6.1 we investigate the relevance of this conclusion to real non-linear networks (cf. to the complementary account in (Li et al., 2020)).

Weight initialization. Different weight initialization schemes have been proposed to stabilize the learning and minimize the hazard of "exploding gradients" (e.g., Glorot & Bengio, 2010; He et al., 2015). Our analysis (see Appendix A) identifies a related variant, which eliminates the hazard when all the hidden layers are of equal width.

Slower convergence with random labels. Zhang et al. (2016) showed that neural networks can learn any label assignment, but they converge faster when seeing true labels as compared to random labels. We report a similar phenomenon when training deep linear networks. In these models, our analysis shows that when the principal eigenvectors are correlated with class identity, as is often the case in real image data, the loss decreases faster when given true label assignments as against random label assignments. In Section 6.2 we investigate this hypothesis empirically in realistic non-linear networks.

1.3. Related Work

Baldi & Hornik (1989) studied the optimization landscape of deep linear models and their relation to PCA. Recent

work suggests that with sufficient over-parameterization, this landscape is well behaved (Kawaguchi, 2016; Zhou & Liang, 2018) and all its local minima are global (Laurent & Von Brecht, 2017). Deep linear networks are also used to study biases induced by architecture or optimization (Ji & Telgarsky, 2018; Wu et al., 2019).

The non-linear dynamics of learning in deep linear networks was studied in (Fukumizu, 1998; Saxe et al., 2013; Arora et al., 2018), analyzing continuous gradients of a regression loss. Here the focus is on the path taken by gradient descent to reach a certain solution, rather than the final outcome. Thus Saxe et al. (2013; 2019) analyzed this model’s dynamics as a function of the input and input-output statistics, and assumed that the data’s singular values are identical (whitened data). **Unfortunately, this assumption obscured the main result of our analysis - the dependence of convergence on singular values.**

Arora et al. (2018) investigate continuous gradients of this model while allowing for a more general loss, **still assuming whitened data.** Although there is some superficial resemblance between their pre-conditioning and our *gradient scale matrices* as defined below, they are defined quite differently and have different properties. Gidel et al. (2019) investigated a similar 2-layer model. Differently from us, both papers assume vanishing initialization.

The elementary two-layer non-linear model with ReLU activation is used in Arora et al. (2019) to track the dynamics of learning with vanishing initialization, revealing a different possible mechanism that may explain the slower convergence of networks when given random labels. Allen-Zhu et al. (2018) present this model as a certain extension of NTK (Jacot et al., 2020). In this framework, convergence is fastest along the largest kernel principal components.

It is often reported that neural network start by learning a simple model (Gunasekar et al., 2018; Soudry et al., 2018; Hu et al., 2020; Nakkiran et al., 2019; Gissin et al., 2019), which gains complexity as learning proceeds, in a phenomenon termed *simplicity bias* (Dingle et al., 2018). Such works often try to explain the extensive generalization capabilities of neural networks (Heckel & Soltanolkotabi, 2019; Ulyanov et al., 2018; Valle-Perez et al., 2018), leaving the precise notion of simplicity vague (Shah et al., 2020).

2. Theoretical Analysis of Elementary Models

2.1. Notations

Let $\mathbb{X} = \{(\mathbf{x}_i, \mathbf{y}_i)\}_{i=1}^n$ denote the training data, where $\mathbf{x} \in \mathbb{R}^q$ denotes the i -th data point and $\mathbf{y} \in \{0, 1\}^K$ its corresponding label. Let $\frac{1}{n_i} \mathbf{m}_i$ denote the centroid (mean) of class i with n_i points, where $\sum_{i=1}^K n_i = n$. Finally, let X and Y denote the matrices whose i th column is \mathbf{x}_i and

\mathbf{y}_i respectively.

Capturing the structure of the data irrespective of class identity, $\Sigma_{XX} = \sum_{i=1}^n \mathbf{x}_i \cdot \mathbf{x}_i^\top = XX^\top$ denotes the uncentered covariance matrix of \mathbb{X} , and $\Sigma_{YX} = \sum_{i=1}^n \mathbf{y}_i \cdot \mathbf{x}_i^\top = YX^\top$ denotes the cross-covariance matrix.

Definition 1 (Principal coordinate system). *The coordinate system obtained by rotating the data in \mathbb{R}^q by an orthonormal matrix U^\top , where $\text{svd}(\Sigma_{XX}) = UDU^\top$.*

In the *principal coordinate system*, $\Sigma_{XX} = D$ is a diagonal matrix whose elements are the singular values of XX^\top , arranged in decreasing order $d_1 \geq d_2 \geq \dots \geq d_q \geq 0$.

Let $f(\mathbf{x})$ denote a linear network. Then

$$f(\mathbf{x}) = \left(\prod_{l=L}^1 W_l \right) \mathbf{x} = \mathbf{W}\mathbf{x}, \quad \mathbf{W} \in \mathbb{R}^{K \times q}$$

We call \mathbf{W} the *compact representation* of the network.

Definition 2 (Error matrix). *For a linear network represented by matrix \mathbf{W} , its error matrix is defined as*

$$Er = \mathbf{W}\Sigma_{XX} - \Sigma_{YX} \quad (1)$$

In the principal coordinate system, the error matrix becomes $Er = \mathbf{W}D - M$, where $M = [\mathbf{m}_1 \dots \mathbf{m}_K]^\top$.

2.2. Deep Linear Network: Framework & Highlights

We show below (Eq. 6) that the change in the network’s compact representation \mathbf{W}^s at time s is the following:

$$\mathbf{W}^{s+1} = \mathbf{W}^s - \mu \sum_{l=1}^L A_l^s \cdot Er^s \cdot B_l^s \quad (2)$$

where μ denotes the learning rate. We use the *gradient scale matrices* notation introduced in (7), where $B_l^s \in \mathbb{R}^{q \times q}$ and $A_l^s \in \mathbb{R}^{K \times K}$. When the number of hidden layers is 0 ($L = 1$), both reduce to the identity matrix and the dynamics in (2) is reduced to the following known result (e.g., Sara & Solla, 1991)

$$\mathbf{W}^{s+1} = \mathbf{W}^s - \mu Er^s \quad (3)$$

Gradient scale matrices. The difference between the multi-layer and single-layer dynamics is captured by the two *gradient scale matrices* A_l^s and B_l^s . Some statistical properties of such matrices are established in Appendix A. Note that the objective function when training a linear network (with no hidden layers) is convex, and therefore its optimization by gradient descent is well understood. Not surprisingly, therefore, our analysis reveals that the dynamics of these matrices captures, and indeed explains, the dynamics of learning in over-parameterized deep linear models.

Assumptions. Our analysis assumes that the learning rate μ is infinitesimal, and therefore terms of size $O(\mu^2)$ can be neglected. We further assume that the width of intermediate layers is approximately equal to a very large number m , and that terms of size $O(\frac{1}{m})$ can also be neglected. In Section 2.4, these assumptions are shown to be reasonable: we see the predicted dynamics throughout the training of deep linear networks of moderate width.

A matter of scale. The theoretical results described in Appendix A rely on a weight initialization scheme reminiscent of Glorot initialization. This scheme guarantees, in fact, that the two *gradient scale matrices* are as close as possible to the identity matrix at the beginning of training, and that further changes in scale are minimized. We therefore submit that this initialization is optimally suitable to reduce the risk of "exploding gradients" when using gradient descent.

Convergence. In Section 2.3 we analyze the evolution of the *gradient scale matrices* as learning proceeds, theoretically justifying the empirical observation that B_l^s changes very slowly away from the identity matrix as s increases. The change in A_l^s is still small, but significantly larger than B_l^s when the number of classes is much smaller than the dimension of the data ($K \ll q$), the case with image data.

Dynamics in the extreme. Let \mathbf{W} denote the network's compact representation using the coordinate system defined in Def. 1, and let \mathbf{w}_j denote its j -th column. When the size of intermediate layers m is large enough so that we can neglect terms of size $O(\frac{1}{m})$, the following holds:

$$\mathbf{w}_j^{s+1} = \lambda_j^s \mathbf{w}_j^0 + (1 - \lambda_j^s) \mathbf{w}_j^{opt} \quad (4)$$

where $\lambda_j = (1 - \mu L d_j)$.

Eq. 4 is reminiscent of the well understood dynamics of training the convex one layer linear model. (4) is composed of two additive terms, revealing two parallel and independent processes that take place during gradient descent:

1. The dependence on random initialization diminishes by way of the first term, which tends to 0 exponentially with decline rate λ_j^s .
2. Convergence to the final value is achieved by way of the second term, a geometrical series with common ratio $(1 - \lambda_j^s)$.

In either case, convergence is fastest for the largest singular eigenvalue, or the first column of \mathbf{W} , and slowest for the smallest singular value. In other words, the variance due to random initialization diminishes exponentially faster along directions corresponding to higher principal directions, while convergence to the optimal solution is also exponentially faster along these directions. This implication

can be visualized in Fig. 2. Importantly, the rate of convergence depends on the singular value d_j , corresponding to column j , the number of layers L , and the learning rate μ .

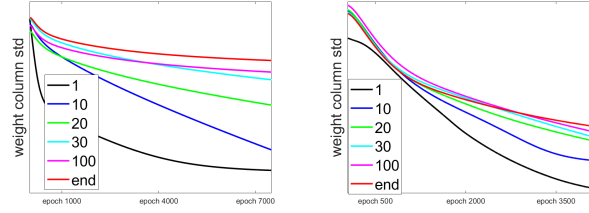


Figure 2. Empirical confirmation of the theoretical results reported below, showing the std of \mathbf{w}_j over 10 independently trained networks as a function of epoch, for 6 different principal components identified by j (see legend). Left: one-layer linear network. Right: two-layer non-linear network with ReLU activation.

2.3. The Dynamics of Deep Linear Network

Consider a deep linear network with L layers, and let

$$L(\mathbb{X}) = \frac{1}{2} \|\mathbf{W}\mathbf{X} - \mathbf{Y}\|_F^2 \quad \mathbf{W} \doteq \prod_{l=L}^1 \mathbf{W}_l \quad (5)$$

$$\mathbf{W}_l \in \mathbb{R}^{m_l \times m_{l-1}}, \quad \mathbf{W}_1 \in \mathbb{R}^{m_1 \times q}, \quad \mathbf{W}_L \in \mathbb{R}^{K \times m_{L-1}}$$

Above m_l denotes the number of neurons in hidden layer l , where $m_0 = q$ and $m_L = K$.

Theorem 1. *The compact matrix representation \mathbf{W} , which succinctly describes a deep linear network, obeys the following dynamics*

$$\mathbf{W}^{s+1} = \mathbf{W}^s - \mu \sum_{l=1}^L A_l^s \cdot \text{Er}^s \cdot B_l^s + O(\mu^2) \quad (6)$$

where Er^s is defined in (1) and

$$A_l^s \doteq \left(\prod_{j=L}^{l+1} \mathbf{W}_j^s \right) \left(\prod_{j=L}^{l+1} \mathbf{W}_j^s \right)^\top \in \mathbb{R}^{K \times K} \quad (7)$$

$$B_l^s \doteq \left(\prod_{j=l-1}^1 \mathbf{W}_j^s \right)^\top \left(\prod_{j=l-1}^1 \mathbf{W}_j^s \right) \in \mathbb{R}^{q \times q}$$

A_l^s and B_l^s are called *gradient scale matrices*.

The proof can be found in App. B.1.

Initially for $s = 0$, random matrices $\mathbf{W}_l^0 \in \mathbb{R}^{m_l \times m_{l-1}}$ are sampled iid from a distribution with mean 0 and variance σ_l^2 . Let \mathfrak{m} denote the width of the smallest hidden layer, $\mathfrak{m} = \min(m_1, \dots, m_{L-1})$, and assume that $\max(m_1, \dots, m_{L-1}) - \min(m_1, \dots, m_{L-1})$ is bounded by some M_b as $\mathfrak{m} \rightarrow \infty$. Assume the following weight initialization scheme (see §A.1 for justification):

$$\forall 1 < l < L : \sigma_l^2 = \frac{2}{m_{l-1} + m_l}, \quad \sigma_1^2 = \frac{1}{m_1}, \quad \sigma_L^2 = \frac{1}{m_{L-1}}$$

At each time s , let $A_l^s(\mathfrak{m})$ and $B_l^s(\mathfrak{m})$ denote a sequence of random *gradient scale matrices*, corresponding to networks whose smallest hidden layer has \mathfrak{m} neurons. From Appendix A we can deduce the following theorem:

Theorem 2. $\forall s$

$$B_l^s(\mathfrak{m}) \xrightarrow{p} I + O(\mu^2), \quad \text{var}[B^l(\mathfrak{m})] = O\left(\frac{1}{\mathfrak{m}}\right)$$

$$A_l^s(\mathfrak{m}) \xrightarrow{p} I + O(\mu^2), \quad \text{var}[A^l(\mathfrak{m})] = O\left(\frac{1}{\mathfrak{m}}\right)$$

where \xrightarrow{p} denotes convergence in probability.

Proof. Proof by induction on s . Initially when $s = 0$, the claim follows from Thm 4 and Corr 5.1. The induction step validity follows from Thm 6 and Thm 7 (see §A.2).

The term $O(\mu^2)$ emerges since the analysis in Appendix A is infinitesimal: when comparing (16) with (6), $\Delta \mathbf{W}^s$ is matched with $\Delta \mathbf{Q}^l + O(\mu^2)$ for a suitable choice of l . \square

Corollary 2.1. $\forall \epsilon, \delta > 0 \exists \mathfrak{m}_b \in \mathbb{N}$, such that $\forall \mathfrak{m} > \mathfrak{m}_b$

$$P(|B_l^s - I| > \epsilon) < \delta$$

and $\exists \mathfrak{m}_a \in \mathbb{N}$, such that $\forall \mathfrak{m} > \mathfrak{m}_a$

$$P(|A_l^s - I| > \epsilon) < \delta$$

Thus, if the width of the smallest hidden layer \mathfrak{m} is large, $B_l^s \approx I$ and $A_l^s \approx I \forall l, s$.

Convergence rate. As shown in §A.2, the convergence of B_l^s to I is governed by $O\left(\frac{K}{\mathfrak{m}}\right)$, while the convergence of A_l^s is governed by $O\left(\frac{q}{\mathfrak{m}}\right)$. Recall that \mathfrak{m} is the size of the smallest hidden layer, which is typically very large, q is the dimension of the data space, which is fixed in advance and can be fairly large, and K is the number of classes, which is fixed and quite small. Typically, $K \ll q$. Thus we expect the right *gradient scale matrices* B_l^s to remain approximately I much longer than the left matrices A_l^s .

Empirical validation. Since the results above are asymptotic, and in order to envision the difference between convergence governed by $O\left(\frac{K}{\mathfrak{m}}\right)$ vs. $O\left(\frac{q}{\mathfrak{m}}\right)$, we resort to simulations of deep linear networks. Accordingly, in Section 2.4 we demonstrate that the *gradient scale matrices* remain approximately I when training linear models of reasonable width and depth. The difference between the convergence rate of B_l^s and A_l^s is clearly seen in Fig. 3, where ΔA_l^s starts to increase shortly before convergence, while ΔB_l^s remains essentially 0 throughout.

2.3.1. WEIGHT EVOLUTION

We now shift to the principal coordinate system defined in Def 1. In this representation $Er^s = \mathbf{W}^s D - M$, where $D = \text{diag}(\{d_j\}_{j=1}^q)$ is a diagonal matrix. Based on Corr 2.1 and the subsequent discussion of convergence rate, assuming that the width of the hidden layers is very large, we can readily substitute $B_l^s \approx I \forall l$ in (6), to obtain

$$\mathbf{W}^{s+1} = \mathbf{W}^s - \mu \sum_{l=1}^L A_l^s Er^s + O(\mu^2) \quad (8)$$

Let $\mathbf{w}_j \in \mathbb{R}^K$ denote the j -th column of \mathbf{W} , \mathbf{m}_j denote the j -th column of M . From (8) we have

$$\mathbf{w}_j^{s+1} = \mathbf{w}_j^s - \mu \sum_{l=1}^L A_l^s (d_j \mathbf{w}_j^s - \mathbf{m}_j) \quad j \in [K]$$

This is a telescoping series; denoting $A^s = \sum_{l=1}^L A_l^s$,

$$\begin{aligned} \mathbf{w}_j^{s+1} &= \mathbf{w}_j^s - \mu A^s (d_j \mathbf{w}_j^s - \mathbf{m}_j) \\ &= (I - \mu d_j A^s) \mathbf{w}_j^s + \mu A^s \mathbf{m}_j \\ &= \dots \\ &= \prod_{\nu=1}^s (I - \mu d_j A^\nu) \mathbf{w}_j^0 \\ &\quad + \mu \left[\sum_{\nu=1}^s \prod_{\rho=\nu+1}^s (I - \mu d_j A^\rho) A^\nu \right] \mathbf{m}_j \end{aligned} \quad (9)$$

The only difference between individual columns lies in d_j , which governs the rate of convergence of the first term to 0, and the rate of convergence of the second term to the optimal value of $\frac{1}{d_j} \mathbf{m}_j$.

In the discussion following the proof of Thm 2, we noted that the approximation $A_l^s \approx I$ breaks down before $B_l^s \approx I$. While it is still valid, (9) becomes

$$\begin{aligned} \mathbf{w}_j^{s+1} &= (1 - \mu d_j L)^s \mathbf{w}_j^0 + \mu \left[\sum_{\nu=1}^s (1 - \mu d_j L)^{(s-\nu)} L I \right] \mathbf{m}_j \\ &= \lambda_j^s \mathbf{w}_j^0 + \mu L \left[\sum_{k=0}^{s-1} \lambda_j^k \right] \mathbf{m}_j \quad \lambda_j = 1 - \mu d_j L \\ &= \lambda_j^s \mathbf{w}_j^0 + (1 - \lambda_j^s) \frac{\mathbf{m}_j}{d_j} \end{aligned} \quad (10)$$

2.3.2. DISCUSSION

The convergence pattern that emerges is governed by the statistics of the data: when aligning the data with the *Principal coordinate system* (Def. 1), the convergence rate of each column of \mathbf{W} , the compact representation of the network, is exponentially decreasing at a rate $\lambda_j = (1 - \mu L d_j)$,

which is governed by the corresponding singular values d_j . At the beginning of training, and when some mild conditions are met, two parallel processes seem to take place: (i) The first term in (10) implies an exponential decline in the contribution of the random initialization w_j^0 , at a rate of λ_j . (ii) The second term in (10) implies that the weight vector converges to its optimal value $\frac{1}{d_j} \mathbf{m}_j$ as a geometric series, whose common ratio is similarly λ_j . Together they imply that weight columns corresponding to higher eigenvectors converge faster. Moreover, fixing the learning rate μ , convergence rate increases linearly with depth L .

2.4. Gradient Scale Matrices: Empirical Validation

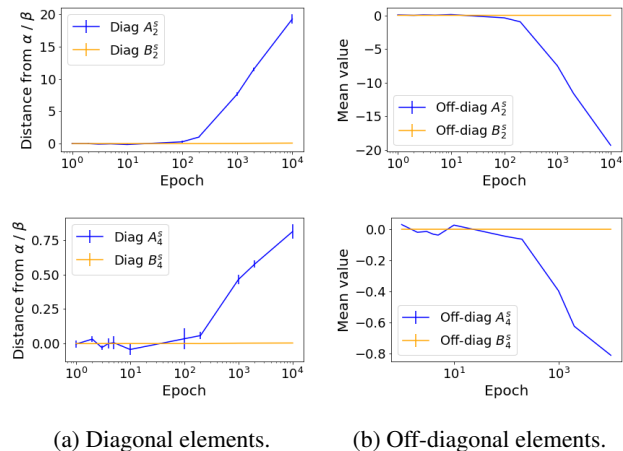


Figure 3. Empirical evaluation of A_l^s and B_l^s , for a 5-layered fully connected linear network, trained on the small-mammals dataset. (a) Mean distance of the diagonal elements of A_l^s and B_l^s from α_l^s and β_l^s respectively. (b) Mean value of the off-diagonal elements of A_l^s and B_l^s . We show layer 2 (top) and 4 (bottom); the remaining 3 layers are almost identical.

The results above indicate that with the assumed weight initialization, the *gradient scale matrices* tend to the identity matrix $\forall s$. We also showed that the right *gradient scale matrix* B_l^s is less likely to change significantly with time. This asymptotic analysis relied on the width of the hidden layers being large enough, and the learning rate small enough. To validate these assumptions, we now investigate empirically the evolution of these matrices throughout the learning.

To this end we trained 10 5-layered linear networks on the small mammals dataset, and computed for each epoch s and each layer l the mean and std of the diagonal and off-diagonal elements of the gradient scale matrices A_l^s, B_l^s . Results for two typical layers are show in Fig. 3. We can see that up to epoch 200, both matrices are almost diagonal: the off-diagonal values are approximately 0, with very low std, and the mean of each diagonal element is approximately α_l for A_l^s and β_l for B_l^s (see definition in Thm 3), with very low std. We note that at the point of divergence, the

networks have already converged, reaching their maximal test performance in epoch 200 as well.

2.5. Adding Non-Linear ReLU Activation

We now analyze a relatively simple non-linear model introduced in (Arora et al., 2019), here adapted to classification rather than regression. This is a two-layer model with ReLU activation, where only the weights of the first layer are being learned. Similarly to (5), the loss is defined as

$$L(\mathbb{X}) = \frac{1}{2} \sum_{i=1}^n \|f(\mathbf{x}_i) - \mathbf{y}_i\|^2$$

$$f(\mathbf{x}_i) = \mathbf{a}^\top \cdot \sigma(W\mathbf{x}_i), \quad \mathbf{a} \in \mathbb{R}^m, \quad W \in \mathbb{R}^{m \times d}$$

m denotes the number of neurons in the hidden layer. We consider a binary classification problem with 2 classes, where $y_i = 1$ for $\mathbf{x}_i \in C_1$, and $y_i = -1$ for $\mathbf{x}_i \in C_2$. $\sigma(\cdot)$ denotes the ReLU activation function applied element-wise to vectors, where $\sigma(u) = u$ if $u \geq 0$, and 0 otherwise.

In App. B.2 we show that, under certain assumptions,

$$W^{s+1} - W^s \approx -\mu \frac{1}{2} \left[(\mathbf{a}\mathbf{a}^\top) W^s \Sigma_{XX} - \tilde{M}^s \right] \quad s < s'$$

where \tilde{M}^s denotes the matrix whose r -th row is $a_r \tilde{\mathbf{m}}_r^s$, and s' a fixed epoch. This equation is reminiscent of (3), and we may conclude that when it holds and using the principal coordinate system, the rate of convergence of the j -th column of W^s is governed by the singular value d_j .

This theoretical result makes some unrealistic assumptions. Reassuringly, empirical results, shown in Fig. 2, indicate that the analysis is valid beyond the assumed circumstances.

3. PC-Bias: Empirical Study

In this section we investigate the dynamics of learning in deep linear and non-linear networks, focusing on its connection to eigendecomposition in light of the results described above. Firstly, when analyzing deep linear networks, we show that convergence rate is indeed governed by the principal singular values of the data, which demonstrates the plausibility of the assumptions made in Section 2. In fact, some assumptions can be relaxed – we can replace the L_2 loss with the more commonly used cross-entropy, and use SGD instead of the deterministic GD. Secondly, we show that the same behavior is observed during the early stages of learning even in non-linear neural networks.

3.1. Methodology

A network is L -layered when it has $L - 1$ hidden layers. Each linear layer is fully connected, and contains 1024 weights, initialized with Glorot uniform initialization. Using a different number of neurons at each layer resulted in

similar qualitative results. All networks are trained using an SGD optimizer, without momentum or L_2 regularization. In all the experiments, learning rate was coarsely grid-searched to minimize a validation error. Hyper-parameters were arbitrarily chosen, with similar results for other choices.

Although the theoretical results are proved for the L_2 loss, in this empirical evaluation we use the more prevalent cross-entropy loss. Our results show that the *PC-bias* is still valid and governs convergence. We note that all the results hold for the L_2 loss as well, as predicted. When training non-linear networks, we use either VGG-19 (Simonyan & Zisserman, 2014), or a smaller stripped version of it, denoted st-VGG (see architecture description in App. D.2).

The datasets used in the following experiments include STL10, ImageNet-20 (Russakovsky et al., 2015), CIFAR-10 (Krizhevsky et al., 2009) and subsets of CIFAR-10/100 termed *small mammals* for multi-class classification, and *cats and dogs* for binary classification (see §D.3).

3.2. PC-Bias in Deep Linear Networks

We trained 10 L -layered ($L = 1, 2, 5$) linear networks, computed the compact representation \mathbf{W} of each network, and rotated it to align with the canonical coordinate system (Def. 1). Note that each row w_r in \mathbf{W} defines the one-vs-all separating hyperplane corresponding to class r .

To examine both the variability between models and their convergence rate, we inspect w_r at different time points throughout the learning process. The rate of convergence can be measured directly, by observing the change in the weights of each element in w_r . These weight values² should be compared to the optimal values in each row w_r of $W_{opt} = YX^T(XX^T)$. The variability between models is measured by calculating the standard deviation (std) of each w_r across N models.

We start with a 2-layered fully connected linear network. At the beginning of learning, weights are initialized uniformly. As learning proceeds, weights corresponding to larger principal components, converge faster (Fig. 4a-top). This faster convergence implies that weights corresponding to larger principal directions exhibit lower variability across models (Fig. 4a-bottom).

Similar behavior can be observed with convolutional linear networks. When analyzing the compact representation of such networks we observe a similar behavior – weights corresponding to larger principal components converge faster to the optimal value, and their variability across models converges faster to 0 (see Fig. 4b). Thus, although the theoretical results are asymptotic, PC-bias is seen throughout

²Note that the weights tend to be larger for smaller principal components, as can be seen in Fig. 4a, epoch 0, top plot.

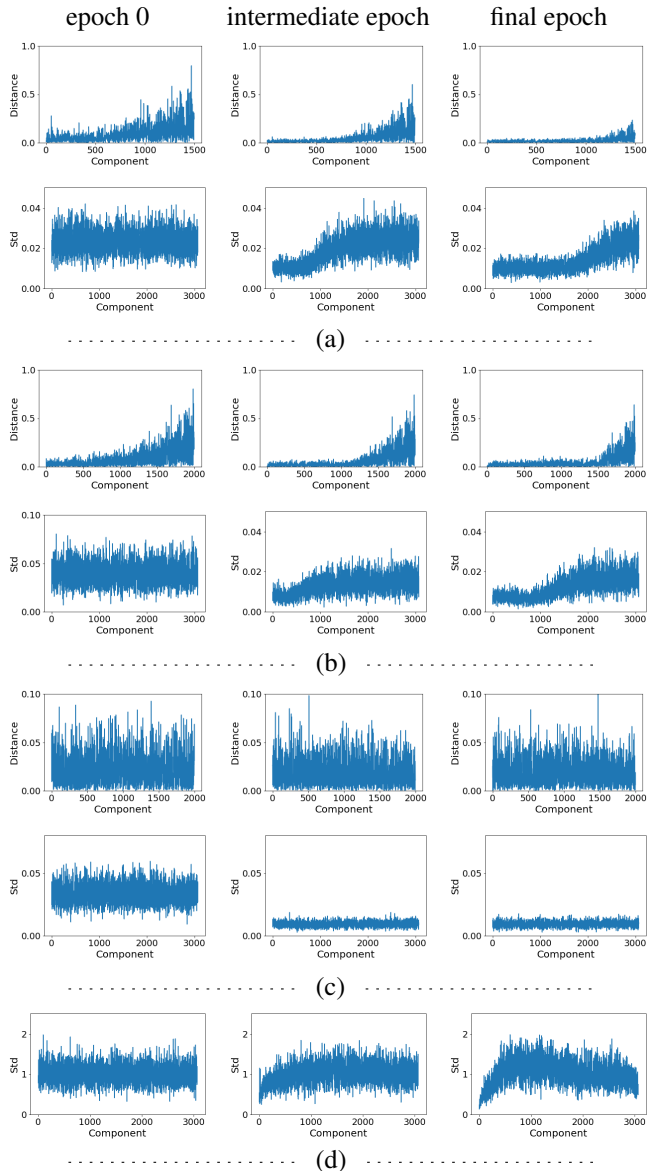


Figure 4. Convergence of the compact representation along the principal directions in different epochs. The value of the X-axis corresponds to the index of a principal eigenvalue, from the most significant to the least significant. (a) 10 2-layered linear networks trained on CIFAR-10. Top: average distance of the weights in w_1 from the optimal linear classifier; bottom: respective std. (b) Similarly, for 10 linear st-VGG networks, trained on the cats and dogs dataset. (c) Similarly, for 10 2-layered linear networks, trained on the cats and dogs dataset, with ZCA-whitening. (d) Similarly, for 10 **non-linear** st-VGG networks trained on the cats and dogs dataset. Here the distance to the optimal solution is not well defined and we therefore only show the std.

the entire learning process of deep linear networks.

Whitened data. The *PC-bias* can no longer be seen when the data is whitened, at which point Σ_{XX} is a scaled identity

matrix. In Fig. 4c, we plot the results of the same experimental protocol while using a ZCA-whitened dataset. As predicted, the networks no longer show any bias towards any principal direction. Weights in all directions are scaled similarly, and the std over all models is the same in each epoch, irrespective of the principal direction.

3.3. PC-Bias in General CNNs

In this section, we investigate the manifestation of the *PC-bias* in non-linear deep CNN networks. We explore two different evaluation frameworks:

Compact representation. Deep CNN networks are highly non-linear, hence we cannot directly track the learning dynamics separately in each principal direction. To this end we need to employ a linear approximation for each network. We considered a number of approximations, but since all of them showed the same qualitative behavior, we describe below the results with the simplest one. Specifically, to obtain a linear approximation of a non-linear network, without dropout or batch-normalization, we follow the definition of the compact representation from Section 2.1 while ignoring any non-linear activation. We then align this matrix with the canonical coordinate system (Def. 1), and observe the evolution of the weights and their std across models along the principal directions during learning. Note that now the networks do not converge to the same compact representation, which is not unique. Nevertheless, we see that the *PC-bias* governs the weight dynamics to a noticeable extent.

More specifically, in these networks, a large fraction of the lowest principal components hardly changes throughout the learning, as good as being ignored, possibly due to the *spectral bias* (see Section 5). Nevertheless, we see the *PC-bias* affecting the higher principal components, most notably at the beginning of training. Thus weights corresponding to higher principal components converge faster, and the std across models of such weights decreases faster for higher principal components (see Fig. 4d).

Projection to higher PC’s. We created a projected dataset using the highest principal components, by projecting each example on the span of the first P principal components. This is equivalent to reducing the dimensions of the dataset to P using PCA. We trained an ensemble of $N=100$ st-VGG networks on the small mammals dataset. We evaluated these networks during training on the same dataset, reduced to $P=1,10,100,1000$ dimensions. The mean accuracy on each dataset throughout the entire learning is plotted in Fig. 5a.

Taking a closer look at Fig. 5a, we see that with fewer projected dimensions where $P=1,10$, the learning curves peak after a few epochs, after which performance decreases and convergence occurs. This result suggests that the networks rely more heavily on these dimensions in the earlier

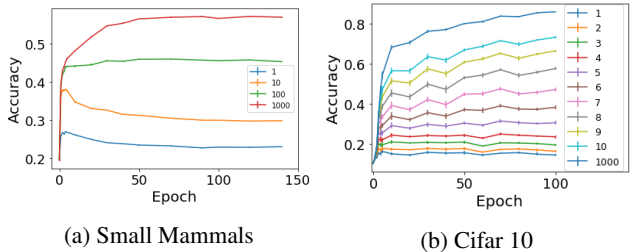


Figure 5. Evaluations on datasets projected to the first P principal components. Each line represents a different value of P . (a) 10 st-VGG networks trained on small mammals; (b) 10 VGG-19 models trained on CIFAR-10.

phases of learning, and then continue to learn other things. On the other hand, with more projected dimensions where $P=100,1000$, the learning curves peak later on, more so for larger P . This delay in convergence suggests that the networks continue to explore the lower principal components, corresponding to larger P , in later stages of the learning.

We repeat this experiment with $N=10$ VGG-19 networks trained on CIFAR-10, with a wider variety of projection sizes P , see Fig. 5b. Once again, in agreement with the *PC-bias* predictions, increasing the number of dimensions P delays convergence.

4. PC-Bias: Learning Order Constancy

In this section we show that the *PC-bias* is largely correlated with the learning order of deep neural networks, and can therefore partially account for the *LOC* effect discussed in Section 1. Following Hacoheh et al. (2020), we measure the “speed of learning” of each example by computing its *accessibility* score. This score characterizes the learning in an ensemble of N networks, trained over E epochs, and computed as the mean accuracy of each example over E and N . Formally:

$$accessibility(\mathbf{x}) = \frac{1}{NE} \sum_{i=1}^N \sum_{e=1}^E \mathbf{1}[f_i^e(\mathbf{x}) = y(\mathbf{x})]$$

where $f_i^e(\mathbf{x})$ denotes the outcome of the i th network trained over e epochs. For the set of datapoints $\{(\mathbf{x}_j, \mathbf{y}_j)\}_{j=1}^n$, *Learning Order Constancy* is manifested by the high correlation between 2 instances of *accessibility*(\mathbf{x}), each computed from a different ensemble.

4.1. Correlating LOC of Linear vs Non-Linear Models

Prevalent networks tend to outperform deep linear networks by a large margin. Importantly, they typically start by learning the same examples, which are correctly recognized by linear models, in the first few training epochs (Hacoheh et al., 2020). To capture the order of learning in the first few epochs, we correlate the order of learning on this set

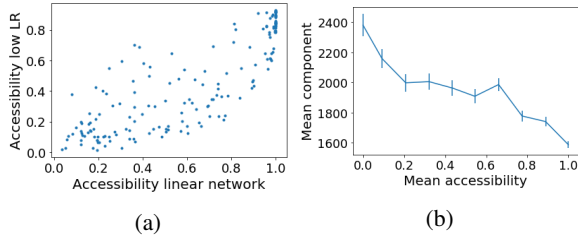


Figure 6. (a) Correlation ($r = 0.85$, $p < 10^{-45}$) between the *accessibility* score of $N=100$ st-VGG networks trained with a low learning rate, and $N=100$ deep linear networks, trained on small mammals. (b) Correlation between the *accessibility* score of $N=100$ st-VGG networks trained on cats and dogs, and the *critical principal component* score. The *accessibility* plot is smoothed by moving average of width 10. Error bars indicate standard error.

of examples, while using drastically reduced learning rates when training the non-linear models.

In accordance, we compare the order of learning of non-linear models and deep linear networks by computing the correlation between the *accessibility* scores of both models. This comparison reveals high correlation, see Fig. 6a, which suggests that observations made when analyzing linear networks are also relevant to non-linear networks.

4.2. PC-Bias is Correlated with LOC

Here we investigate directly the connection between *PC-bias* and LOC. We define the *critical principal component* of an example to be the first principal component P , such that a linear classifier trained on the original data can classify the example correctly when projected to P principal components or more. We trained $N=100$ st-VGG networks on the cats and dogs dataset, and computed for each example its *accessibility* score and its *critical principal component*. In Fig. 6b we see a strong negative correlation between the two scores ($p=-0.93$, $r < 10^{-4}$), suggesting that the *PC-bias* affects the order of learning as measured by *accessibility*.

4.3. Removing the PC-Bias Diminishes LOC

Whitening the data eliminates the *PC-bias* as shown in Fig. 4c, since all the singular values are now identical. Here we use this observation to further probe into the dependency of the *Learning Order Constancy* on the *PC-bias*. Starting with the linear case, we train 4 ensembles of $N=10$ 1-layered linear networks on the cats and dogs dataset, 2 with and 2 without ZCA-whitening. We compute the *accessibility* score for each ensemble separately, and correlate the scores of the 2 ensembles in each test case. Each correlation captures the consistency of the *LOC* effect for the respective condition. This correlation is expected to be very high for natural datasets. Low correlation implies that the *LOC* effect is weak, as training the same network over the same dataset yields a different learning order.

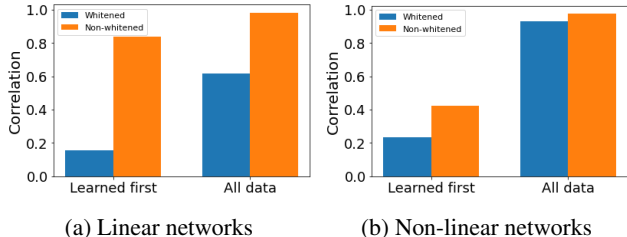


Figure 7. Learning order consistency with and without a *PC-bias*. Each bar represents the correlation between the learning order of 2 collections of 10 networks trained on CIFAR-10. Orange bars represent natural data, in which the *PC-bias* is present, while blue bars represent whitened data, in which the *PC-bias* is eliminated. As *PC-bias* is more prominent at the beginning of the learning, we compare these correlations for the entire data (right 2 bars), and for the subset of 20% "fastest learned" examples (left 2 bars).

Fig. 7a shows these correlations for deep linear networks. The orange bars represent the correlation between the 2 collections of natural images, while the blue bars represent the correlation between the 2 whitened collections. As expected, the correlation when using natural images is very high. However, when using whitened images, correlation plummets, indicating that the *LOC* effect is highly dependent on the *PC-bias*. We note that the drop in the correlation is much higher when considering only the 20% "fastest learned" examples, suggesting that the *PC-bias* affects learning order more at earlier stages of learning.

In Fig. 7b we repeat this experiment with non-linear networks, training 2 collections of $N=10$ VGG-19 networks on CIFAR-10. We find that the elimination of the *PC-bias* in this case affects the *LOC* much less, suggesting that the *PC-bias* can only partially account for the *LOC* effect in the non-linear case. However, we note that at the beginning of learning, when the *PC-bias* is most pronounced, once again the drop is much larger and very significant (half).

5. Spectral Bias: Empirical Study

The *spectral bias*, discussed in Section 1.1, may also partially account for the order of learning of individual examples. In this section we investigate the relation between the *spectral bias* and *accessibility* (Section 5.2), in order to clarify its relation to the *Learning Order Constancy* and the *PC-bias* (Section 5.3). First, however, we expand the scope of the empirical evidence for this effect to the classification scenario and real image data (Section 5.1).

5.1. Spectral Bias in Classification

Rahaman et al. (2019) showed that when regressing a 2D function by a neural network, the model seems to approximate the lower frequencies of the function before its higher

frequencies. Here we extend this empirical observation to the classification formulation. Thus, given frequencies $\kappa = (\kappa_1, \kappa_2, \dots, \kappa_m)$ with corresponding phases $\phi = (\varphi_1, \varphi_2, \dots, \varphi_m)$, we consider the mapping $\lambda : [-1, 1] \rightarrow \mathbb{R}$ given by

$$\lambda(z) = \sum_{i=1}^m \sin(2\pi\kappa_i z + \varphi_i) := \sum_{i=1}^m \text{freq}_i(z) \quad (11)$$

Above κ is strictly monotonically increasing, while ϕ is sampled uniformly.

The classification rule is defined by $\lambda(z) \leq 0$. We created a binary dataset whose points are fully separated by λ . We refer to this dataset as the *frequency dataset*. In App. C.2, we visualize the decision boundary of an st-VGG network trained on this dataset as it evolves with time. The frequency of this separator increases as learning continues, in agreement with the results in regression tasks.

5.2. Spectral Bias: Relation to Accessibility

In order to connect between the learning order, which is defined over examples, and the Fourier analysis of a separator, we define for each example its *critical frequency*, which characterizes the smallest number of frequencies needed to correctly classify the example. To illustrate, consider the *frequency dataset* defined above. Here, the *critical frequency* is defined as the smallest $j \in [m]$ such that $\lambda_j(z) = \sum_{i=1}^j \text{freq}_i(z)$ classifies the example correctly (see Figs. 16a, 16b in the Suppl.).

In this binary classification task, we observe a strong connection between the order of learning and the *critical frequency*. Specifically, we trained $N=100$ st-VGG networks on the *frequency dataset*, and correlated the *accessibility* scores with the *critical frequency* of the examples (see Fig. 8a). We see a strong negative correlation ($r = -0.93$, $p < 10^{-2}$), suggesting that examples whose *critical frequency* is high are learned last by the networks.

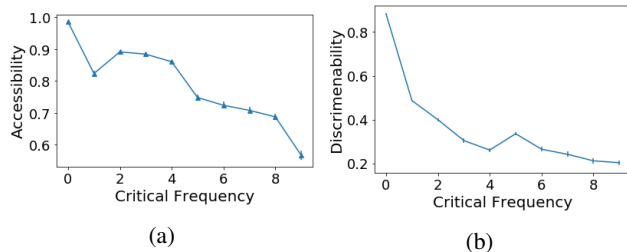


Figure 8. (a) Correlation between *critical frequency* and *accessibility* score in the 2D-frequency dataset. (b) Correlation between *discriminability* and *critical frequency* in the 2D-frequency dataset.

5.3. Spectral-Bias as Explanation to LOC

In order to see the effect of the *spectral bias* in real classification task and extend the above analysis to natural images, we need to define a score which captures the notion of *critical frequency*. To this end we define the *discriminability* measure of an example - the percentage out of its k neighbors that share the same class as the example. Intuitively, an example has a low *discriminability* score when it is surrounded by examples from other classes, which forces the learned boundary to incorporate high frequencies. In Fig. 8b we plot the correlation between the *discriminability* and the *critical frequency* for the 2D frequency dataset. The high correlation ($r=-0.8$, $p < 10^{-2}$) indicates that *discriminability* indeed captures the notion of *critical frequency*.

Next, we trained several networks (VGG and st-VGG, see §D.2) on several real datasets, including small-mammals, STL-10, CIFAR-10/100 and a subset of ImageNet-20. For each network and dataset, we computed the *accessibility* score as well as the *discriminability* of each example. The correlation between these scores is shown in Table 1.

	Raw data	Penultimate layer
Small mammals	0.46	0.85
ImageNet 20	0.01	0.54
CIFAR-100	0.51	0.85
STL10	0.44	0.7

Table 1. Correlation between *accessibility* and *discriminability*.

To begin with, we compute *discriminability* based on distances in the original data space, since *spectral bias* is defined with respect to the raw data. The relevant correlations are shown in the first column of Table 1. We see a low but significant correlation between *accessibility* and *discriminability* when considering the small datasets (small mammals, CIFAR-100 and STL10), but this correlation vanishes when considering the larger ImageNet-20 dataset. This indicates that the *spectral bias* cannot adequately explain the learning order of examples.

How about discriminability in perceptual space? We compute the *discriminability* based on distances in the perceptual space of each network, using the penultimate layer’s embedding of each network, as shown in the right column of Table 1. Clearly, the correlation between *discriminability* in perceptual space and *accessibility* is much higher than before. This suggests a reversed reasoning: **the network learns a representation where the *spectral bias* is evident, but this bias does not necessarily affect its learning before the representation has been learnt.**

5.4. The two layer ReLU model

Basri et al. (2019) proved that *Spectral bias* typifies the training of the elementary two layer ReLU network. Can this

explain the LOC effect in this model? To clarify this point we investigated this model empirically, observing that the LOC effect is evident at the beginning of learning, peaking at the point of overfit, when the test accuracy begins to decline, and subsequently declining. We likewise note the relation between the onset of overfit and the shift of focus in the training process to principal components that correspond to noise, as discussed below in Section 6.1. The *Spectral bias*, in contrast, does not decline at the onset of overfit. Together, these observations seem to indicate that in this simple model, the LOC effect is more readily explained by the *PC-bias* rather than the *Spectral bias*.

6. PC-Bias: Further Implications

Our results show that the convergence of deep over-parameterized linear neural networks is governed by the principal components of the data. In this section, we discuss how these results explain several characteristics of training deep linear networks, and show empirically that many of them characterize non-linear networks as well. In all the experiments described below we used small versions of the VGG network, denoted 'st-VGG' for the non-linear case and 'linear st-VGG' for its linear counterpart. When training on natural datasets, we used subsets of CIFAR-10 and CIFAR-100. All the experiments were reproduced with several datasets, with similar results (see App. C for details).

6.1. Early Stopping and the Generalization Gap

In natural image datasets, it is often assumed that the least significant principal components of the data represent noise (Torralba & Oliva, 2003). When this is the case, our analysis predicts that noise will be learned in later epochs since the most significant principal components are learned first. This implies, in turn, that early stopping should be beneficial under these circumstances. To investigate this prediction, we manipulated a benchmark dataset in order to generate more noise in either the most significant (higher) or least significant (lower) principal components. Our experiments show that both in deep linear and non-linear networks, early stopping becomes more beneficial when the lower principal components are amplified in the training set, and less beneficial when the higher components are amplified, in accordance with the aforementioned prediction. Examples of these noisy images can be seen in Appendix C.

Specifically, we trained 10 linear and non-linear networks on the manipulated images, where (i) the highest 1.5% principal components are amplified; (ii) the lowest 1.5% principal components are amplified. We plot the accuracy over the test set in each case, see Fig. 9a (linear networks) and Fig. 9b (non-linear networks). In both cases early stopping becomes more beneficial when the lowest principal components are amplified, and vice versa when the highest principal com-

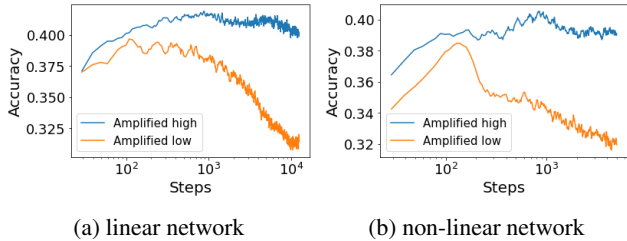


Figure 9. Effects of data amplification in the highest and lowest principal components: (a) linear networks, (b) non-linear networks.

ponents are amplified, which is what we would expect if indeed the noise dominates the lower principal components. This result demonstrates that previous accounts (e.g., Basri et al., 2019; Li et al., 2020) may be insufficient, and supports the hypothesis that the benefit of early stopping, often observed in practice, can be partially attributed to the dependence of convergence on singular values, together with the aforementioned property of natural images.

6.2. Slower Convergence with Random Labels

Zhang et al. (2016) showed that deep neural networks can memorize a dataset perfectly, learning any assignment of random labels to the training data. However, networks trained on randomly labeled data are known to converge much slower (Krueger et al., 2017). Here we show evidence that the same phenomenon occurs in linear networks as well. To account for this, we invoke the same assumption as in Section 6.1, that the lower principal components are dominated by noise in natural image datasets. Consequently, when seeing real labels, as soon as convergence is achieved in the higher principal directions, accuracy is expected to be high. This is no longer the case when labels are shuffled, where accuracy increases more slowly awaiting convergence in the lower principal directions as well. This account is complementary to the one offered in (Arora et al., 2019).

If this account for the slower convergence with shuffled labels is true, it would imply that when the data is whitened the effect should disappear. This is indeed the case in linear networks, see Fig. 10. To further check the relevance of this account to non-linear networks, where this immediate effect is obscured, we artificially generate datasets where only the first P principal components are discriminative, while the remaining components act as noise. We constructed two such datasets: in one the labels are correlated with the original labels, in the other they are not.

Specifically, PCA is used to reduce the dimension of a two-class dataset to P , and the optimal linear separator in the reduced representation is computed. Next, all the labels of points that are incorrectly classified by the optimal linear separator are switched, so that the train and test sets are

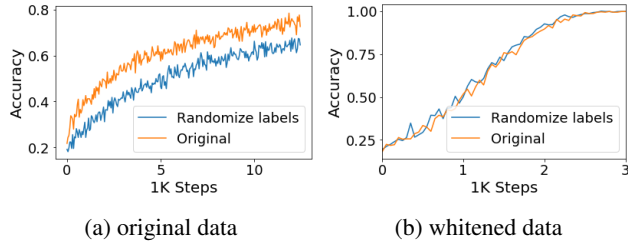


Figure 10. Learning curves of 10 2-layered linear networks, with real and shuffled labels, (a) before and (b) after whitening.

linearly separable by this separator. Note that the modified labels are still highly correlated with the labels before the modification. The second dataset is generated by repeating the process while starting from randomly shuffled labels. This dataset is likewise fully separable when projected to the first P components, but its labels are uncorrelated with the original labels ($p = 0.06$, $r < 10^{-10}$).

We trained 10 non-linear networks with $P=10,50,500$, plotting their mean training accuracy in Fig. 11a (first dataset) and Fig. 11b (second dataset). In both cases, the lower P is (only the first few principal components are discriminative), the faster the data is learned by the non-linear network. Whether the labels are real or shuffled makes little qualitative difference, which supports our proposed account.

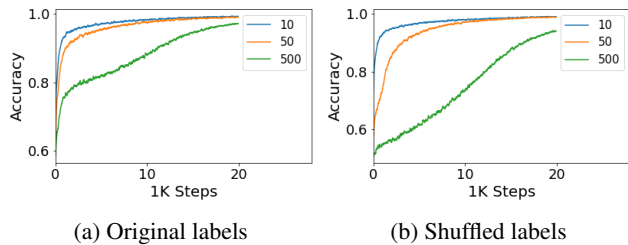


Figure 11. Learning curves when training non-linear networks on 3 modified datasets, which are linearly separable after projection to the highest P principal components (indicated in the legend).

7. Summary

When trained with gradient descent, the convergence rate of the over-parameterized deep linear network model is provably governed by the eigendecomposition of the data, and specifically, parameters corresponding to the most significant principal components converge faster than the least significant components. Empirical evidence is provided for the relevance of these results to more realistic non-linear networks. We term this effect *PC-bias*. This result provides a complementary account for some prevalent empirical observations, including the benefit of early stopping and the slower convergence rate with shuffled labels.

We use the *PC-bias* to explicate the *Learning Order Con-*

stancy (LOC), showing that examples learned at earlier stages are more distinguishable by the higher principal components, and demonstrating that networks rely more heavily on higher principal components early on. A causal link between the *PC-bias* and the *LOC* effect is demonstrated, as the *LOC* effect is diminished when the *PC-bias* is eliminated by introducing whitening. We analyze these findings in view of a related phenomenon termed *spectral bias*. While the *PC-bias* may be more prominent early on, the *spectral bias* may be more important in later stages of learning.

References

- Allen-Zhu, Z., Li, Y., and Liang, Y. Learning and generalization in overparameterized neural networks, going beyond two layers. *arXiv preprint arXiv:1811.04918*, 2018.
- Arora, S., Cohen, N., and Hazan, E. On the optimization of deep networks: Implicit acceleration by overparameterization. In *International Conference on Machine Learning*, pp. 244–253, 2018.
- Arora, S., Du, S., Hu, W., Li, Z., and Wang, R. Fine-grained analysis of optimization and generalization for overparameterized two-layer neural networks. In *International Conference on Machine Learning*, pp. 322–332, 2019.
- Baldi, P. and Hornik, K. Neural networks and principal component analysis: Learning from examples without local minima. *Neural networks*, 2(1):53–58, 1989.
- Basri, R., Jacobs, D. W., Kasten, Y., and Kritchman, S. The convergence rate of neural networks for learned functions of different frequencies. In *Advances in Neural Information Processing Systems*, pp. 4761–4771, 2019.
- Basri, R., Galun, M., Geifman, A., Jacobs, D., Kasten, Y., and Kritchman, S. Frequency bias in neural networks for input of non-uniform density. In *International Conference on Machine Learning*, pp. 685–694. PMLR, 2020.
- Cao, Y., Fang, Z., Wu, Y., Zhou, D.-X., and Gu, Q. Towards understanding the spectral bias of deep learning. *arXiv preprint arXiv:1912.01198*, 2019.
- Dingle, K., Camargo, C. Q., and Louis, A. A. Input–output maps are strongly biased towards simple outputs. *Nature communications*, 9(1):1–7, 2018.
- Fukumizu, K. Effect of batch learning in multilayer neural networks. *Gen*, 1(04):1E–03, 1998.
- Gidel, G., Bach, F., and Lacoste-Julien, S. Implicit regularization of discrete gradient dynamics in linear neural networks, 2019.
- Gissin, D., Shalev-Shwartz, S., and Daniely, A. The implicit bias of depth: How incremental learning drives generalization. *arXiv preprint arXiv:1909.12051*, 2019.

- Glorot, X. and Bengio, Y. Understanding the difficulty of training deep feedforward neural networks. In *Proceedings of the thirteenth international conference on artificial intelligence and statistics*, pp. 249–256, 2010.
- Gunasekar, S., Lee, J., Soudry, D., and Srebro, N. Implicit bias of gradient descent on linear convolutional networks. *arXiv preprint arXiv:1806.00468*, 2018.
- Hacohen, G., Choshen, L., and Weinshall, D. Let’s agree to agree: Neural networks share classification order on real datasets. In *International Conference on Machine Learning*, pp. 3950–3960. PMLR, 2020.
- He, K., Zhang, X., Ren, S., and Sun, J. Delving deep into rectifiers: Surpassing human-level performance on imagenet classification. In *Proceedings of the IEEE International Conference on Computer Vision (ICCV)*, December 2015.
- Heckel, R. and Soltanolkotabi, M. Denoising and regularization via exploiting the structural bias of convolutional generators. *arXiv preprint arXiv:1910.14634*, 2019.
- Hu, W., Xiao, L., Adlam, B., and Pennington, J. The surprising simplicity of the early-time learning dynamics of neural networks. *arXiv preprint arXiv:2006.14599*, 2020.
- Jacot, A., Gabriel, F., and Hongler, C. Neural tangent kernel: Convergence and generalization in neural networks, 2020.
- Ji, Z. and Telgarsky, M. Gradient descent aligns the layers of deep linear networks. *arXiv preprint arXiv:1810.02032*, 2018.
- Kawaguchi, K. Deep learning without poor local minima. *arXiv preprint arXiv:1605.07110*, 2016.
- Krizhevsky, A., Hinton, G., et al. Learning multiple layers of features from tiny images. 2009.
- Krueger, D., Ballas, N., Jastrzebski, S., Arpit, D., Kanwal, M. S., Maharaj, T., Bengio, E., Fischer, A., and Courville, A. Deep nets don’t learn via memorization. 2017.
- Laurent, T. and Von Brecht, J. Deep linear neural networks with arbitrary loss: All local minima are global. *arXiv preprint arXiv:1712.01473*, 2017.
- Li, M., Soltanolkotabi, M., and Oymak, S. Gradient descent with early stopping is provably robust to label noise for overparameterized neural networks. In *International Conference on Artificial Intelligence and Statistics*, pp. 4313–4324. PMLR, 2020.
- Nakkiran, P., Kaplun, G., Kalimeris, D., Yang, T., Edelman, B. L., Zhang, F., and Barak, B. Sgd on neural networks learns functions of increasing complexity. *arXiv preprint arXiv:1905.11604*, 2019.
- Rahaman, N., Baratin, A., Arpit, D., Draxler, F., Lin, M., Hamprecht, F., Bengio, Y., and Courville, A. On the spectral bias of neural networks. In *International Conference on Machine Learning*, pp. 5301–5310. PMLR, 2019.
- Russakovsky, O., Deng, J., Su, H., Krause, J., Satheesh, S., Ma, S., Huang, Z., Karpathy, A., Khosla, A., Bernstein, M., et al. Imagenet large scale visual recognition challenge. *International journal of computer vision*, 115(3): 211–252, 2015.
- Sara, Y. L. C. I. K. and Solla, A. Second order properties of error surfaces learning time and generalization. *Advances in neural information processing systems*, 3:918–924, 1991.
- Saxe, A. M., McClelland, J. L., and Ganguli, S. Exact solutions to the nonlinear dynamics of learning in deep linear neural networks. *arXiv preprint arXiv:1312.6120*, 2013.
- Saxe, A. M., McClelland, J. L., and Ganguli, S. A mathematical theory of semantic development in deep neural networks. *Proceedings of the National Academy of Sciences*, 116(23):11537–11546, 2019.
- Shah, H., Tamuly, K., Raghunathan, A., Jain, P., and Netrapalli, P. The pitfalls of simplicity bias in neural networks. *arXiv preprint arXiv:2006.07710*, 2020.
- Simoncelli, E. P. and Olshausen, B. A. Natural image statistics and neural representation. *Annual review of neuroscience*, 24(1):1193–1216, 2001.
- Simonyan, K. and Zisserman, A. Very deep convolutional networks for large-scale image recognition. *arXiv preprint arXiv:1409.1556*, 2014.
- Soudry, D., Hoffer, E., Nacson, M. S., Gunasekar, S., and Srebro, N. The implicit bias of gradient descent on separable data. *The Journal of Machine Learning Research*, 19(1):2822–2878, 2018.
- Torralba, A. and Oliva, A. Statistics of natural image categories. *Network: computation in neural systems*, 14(3): 391–412, 2003.
- Ulyanov, D., Vedaldi, A., and Lempitsky, V. Deep image prior. In *Proceedings of the IEEE conference on computer vision and pattern recognition*, pp. 9446–9454, 2018.
- Valle-Perez, G., Camargo, C. Q., and Louis, A. A. Deep learning generalizes because the parameter-function map is biased towards simple functions. *arXiv preprint arXiv:1805.08522*, 2018.
- Wu, Y., Póczos, B., and Singh, A. Towards understanding the generalization bias of two layer convolutional linear

classifiers with gradient descent. In *The 22nd International Conference on Artificial Intelligence and Statistics*, pp. 1070–1078. PMLR, 2019.

Zhang, C., Bengio, S., Hardt, M., Recht, B., and Vinyals, O. Understanding deep learning requires rethinking generalization. *arXiv preprint arXiv:1611.03530*, 2016.

Zhou, Y. and Liang, Y. Critical points of linear neural networks: Analytical forms and landscape properties. In *Proc. Sixth International Conference on Learning Representations (ICLR)*, 2018.

Appendix

A. Random Matrices

A.1. Multiplication of Random Matrices

In this section we present and prove some statistical properties of general random matrices and their multiplications. Let $\{Q_n \in \mathbb{R}^{m_n \times m_{n-1}}\}_{n=1}^N$ denote a set of random matrix whose elements are sampled iid from a distribution with mean 0 and variance σ_n^2 , with bounded kurtosis. Let

$$\begin{aligned} \mathbf{Q}^l &= \prod_{n=l-1}^1 Q_n = Q_{l-1} \cdots \cdots Q_1 \\ B^l &= \mathbf{Q}^l \mathbf{Q}^{l\top} \in \mathbb{R}^{m_0 \times m_0} \quad l \in [2 \dots N] \end{aligned}$$

and

$$\begin{aligned} \mathbf{Q}^l &= \prod_{n=N}^{l+1} Q_n = Q_N \cdots \cdots Q_{l+1} \\ A^l &= \mathbf{Q}^l \mathbf{Q}^{l\top} \in \mathbb{R}^{m_N \times m_N} \quad l \in [1 \dots N-1] \end{aligned}$$

Theorem 3. $\forall l$

$$\mathbb{E}(B^l) = \beta_l I \quad \beta_l = \prod_{n=1}^{l-1} m_n \sigma_n^2 \quad (12)$$

$$\mathbb{E}(A^l) = \alpha_l I \quad \alpha_l = \prod_{n=l+1}^N m_{n-1} \sigma_n^2 \quad (13)$$

Proof. We only prove (12), as the proof of (13) is similar. To simplify the presentation, we use the following auxiliary notations: $V = Q_1$, $U = \prod_{n=l-1}^2 Q_n \implies \mathbf{Q}^l = UV$.

Proof proceeds by induction on l .

- $l = 2$:

$$\begin{aligned} \mathbb{E}[B_{ij}^l] &= \mathbb{E}\left[\sum_{k=1}^{m_1} V_{ki} V_{kj}\right] \stackrel{i \neq j}{=} \sum_{k=1}^{m_1} \mathbb{E}[V_{ki}] \mathbb{E}[V_{kj}] \\ \mathbb{E}[B_{ii}^l] &= \mathbb{E}\left[\sum_{k=1}^{m_1} V_{ki} V_{ki}\right] = \sum_{k=1}^{m_1} \mathbb{E}[V_{ki}^2] \end{aligned}$$

Thus

$$\mathbb{E}[B_{ij}^l] = \begin{cases} 0 & i \neq j \quad (\text{off diagonal}) \\ m_1 \sigma_1^2 & i = j \quad (\text{diagonal}) \end{cases}$$

- Assume that (12) holds for $l-1$.

$$B_{ij}^l = \sum_k \mathbf{Q}_{ki}^l \mathbf{Q}_{kj}^l = \sum_k \sum_{\nu} U_{k\nu} V_{\nu i} \sum_{\rho} U_{k\rho} V_{\rho j}$$

and therefore

$$\begin{aligned} \mathbb{E}[B_{ij}^l] &= \sum_k \sum_{\nu} \sum_{\rho} \mathbb{E}[U_{k\nu} V_{\nu i} U_{k\rho} V_{\rho j}] \\ &= \sum_{\nu} \sum_{\rho} \mathbb{E}[V_{\nu i} V_{\rho j}] \sum_k \mathbb{E}[U_{k\nu} U_{k\rho}] \end{aligned}$$

where the last transition follows from the independence of U and V . Once again, we consider the diagonal and off-diagonal elements separately. If $i \neq j$:

$$\mathbb{E}[B_{ij}^l] = \sum_{\nu} \sum_{\rho} \mathbb{E}[V_{\nu i}] \mathbb{E}[V_{\rho j}] \sum_k \mathbb{E}[U_{k\nu} U_{k\rho}] = 0$$

If $i = j$:

$$\begin{aligned} \mathbb{E}[B_{ii}^l] &= \sum_{\nu} \sum_{\rho} \mathbb{E}[V_{\nu i} V_{\rho j}] \mathbb{E}[(U^{\top} U)_{\nu\rho}] \\ &= \sum_{\nu} \mathbb{E}[V_{\nu i}^2] \mathbb{E}[(U^{\top} U)_{\nu\nu}] \end{aligned}$$

Using the induction assumption

$$\mathbb{E}[B_{ij}^l] = \begin{cases} 0 & i \neq j \quad (\text{off diagonal}) \\ m_1 \sigma_1^2 \prod_{n=2}^{l-1} m_n \sigma_n^2 & i = j \quad (\text{diagonal}) \end{cases}$$

from which (12) follows. \square

Let m denote the width of the smallest hidden layer, $m = \min(m_1, \dots, m_{N-1})$, and assume that $\max(m_1, \dots, m_{N-1}) - \min(m_1, \dots, m_{N-1})$ is bounded by some M_b as $m \rightarrow \infty$. Assume the following initialization scheme

Definition 3. The elements of $\{Q_n\}_{n=1}^N$ are chosen iid from a distribution with mean 0 and variance σ_n^2 , where

$$\sigma_n^2 = \frac{2}{m_{n-1} + m_n} \quad 1 < n < N, \quad \sigma_1^2 = \frac{1}{m_1}, \quad \sigma_N^2 = \frac{1}{m_{N-1}}$$

For large m , it follows that

$$\begin{aligned} m_n \sigma_n^2 &= 1 + O\left(\frac{1}{m}\right) & n \in [1 \dots N-1] \\ m_{n-1} \sigma_n^2 &= 1 + O\left(\frac{1}{m}\right) & n \in [2 \dots N] \end{aligned}$$

Corollary 3.1. *With initialization as in Def. 3, $\forall l$*

$$\mathbb{E}(B^l) = [1 + O\left(\frac{1}{\mathfrak{m}}\right)]I, \quad \mathbb{E}(A^l) = [1 + O\left(\frac{1}{\mathfrak{m}}\right)]I$$

Theorem 4. *With initialization as in Def. 3, $\forall l$*

$$\text{var}(B^l) = O\left(\frac{1}{\mathfrak{m}}\right), \quad \text{var}(A^l) = O\left(\frac{1}{\mathfrak{m}}\right)$$

Proof. We prove by induction on l that:

$$\begin{aligned} \mathbb{E}[(B_{ij}^l)^2] &= \begin{cases} O\left(\frac{1}{\mathfrak{m}}\right) & i \neq j \quad (\text{off diagonal}) \\ 1 + O\left(\frac{1}{\mathfrak{m}}\right) & i = j \quad (\text{diagonal}) \end{cases} \\ \mathbb{E}[B_{ii}^l B_{jj}^l] &= 1 + O\left(\frac{1}{\mathfrak{m}}\right) \end{aligned} \quad (14)$$

For $l = 2$, (14) follows from Lemma 2 and Corr 3.1. We now assume that (14) holds for $l - 1$ and prove for l , using notations as above: $V = Q_1$, $U = \prod_{l=1}^2 Q_n$, $Q^l = UV$.

$$\mathbb{E}[(B_{ij}^l)^2] = \sum_{\nu, \rho} \sum_{\alpha, \beta} \mathbb{E}[V_{\nu i} V_{\rho j} V_{\alpha i} V_{\beta j} \sum_{k, n} U_{k\nu} U_{k\rho} U_{n\alpha} U_{n\beta}]$$

Let $B^l = U^\top U$. Using the induction assumption

$$\mathbb{E}[(B_{ij}^l)^2] \stackrel{i \neq j}{=} \sum_{\nu, \rho} \mathbb{E}[V_{\nu i}^2 V_{\nu j}^2] \mathbb{E}[(B_{\nu\rho}^{l-1})^2] = O\left(\frac{1}{\mathfrak{m}}\right)$$

When $i = j$, there are three cases where the terms in the sum above do not equal 0: (i) $\nu = \alpha$, $\rho = \beta$, $\nu \neq \rho$ or $\nu = \beta$, $\rho = \alpha$, $\nu \neq \rho$; (ii) $\nu = \rho$, $\alpha = \beta$, $\nu \neq \alpha$; (iii) $\nu = \rho = \alpha = \beta$. (i) is similar to the above, and we therefore only expand cases (ii) and (iii) next:

$$(ii) \sum_{\nu, \alpha} \mathbb{E}[V_{\nu i}^2 V_{\alpha i}^2] \mathbb{E}[B_{\nu\nu}^{l-1} B_{\alpha\alpha}^{l-1}] = 1 + O\left(\frac{1}{\mathfrak{m}}\right)$$

$$(iii) \sum_{\nu} \mathbb{E}[V_{\nu i}^4] \mathbb{E}[(B_{\nu\nu}^{l-1})^2] = O\left(\frac{1}{\mathfrak{m}}\right)$$

In the derivation of (iii) we exploited the assumption that the kurtosis of the distribution used to sample Q_n is fixed at G and cannot depend on \mathfrak{m} , indicating that $\mathbb{E}[V_{\nu i}^4] = G\sigma_1^4$.

A similar argument would show that $\mathbb{E}[B_{ii}^l B_{jj}^l] = 1 + O\left(\frac{1}{\mathfrak{m}}\right)$. \square

Theorem 5. *Let $\{X(\mathfrak{m})\}$ denote a sequence of random matrices where $\mathbb{E}[X(\mathfrak{m})] = [1 + O\left(\frac{1}{\mathfrak{m}}\right)]I$ and $\text{var}[X(\mathfrak{m})] = O\left(\frac{1}{\mathfrak{m}}\right)$. Then*

$$X(\mathfrak{m}) \xrightarrow{P} I$$

where \xrightarrow{P} denotes convergence in probability.

Proof. We need to show that $\forall \epsilon, \delta > 0 \exists \mathfrak{m}' \in \mathbb{N}$, such that $\forall \mathfrak{m} > \mathfrak{m}'$

$$P(|X(\mathfrak{m}) - I| > \epsilon) < \delta$$

Henceforth we use X as shorthand for $X(\mathfrak{m})$. Since $\mathbb{E}(X) = [1 + O\left(\frac{1}{\mathfrak{m}}\right)]I$, it follows that $\forall \epsilon > 0 \exists \mathfrak{m}_1 \in \mathbb{N}$ such that $\forall \mathfrak{m} > \mathfrak{m}_1$, the following holds element-wise:

$$|\mathbb{E}(X) - I| < \frac{\epsilon}{2}$$

Thus

$$P(|X - I| > \epsilon) \leq P(|X - \mathbb{E}(X)| > \frac{\epsilon}{2})$$

Since $\text{var}(X) = O\left(\frac{1}{\mathfrak{m}}\right)$, it follows that $\forall \epsilon, \delta > 0$, $\exists \mathfrak{m}_2 \in \mathbb{N} \ni \forall \mathfrak{m} > \mathfrak{m}_2$

$$\text{var}(X) < \frac{\epsilon^2}{4} \delta$$

From the above, and using Chebyshev inequality

$$P(|X - I| > \epsilon) < \frac{4\text{var}(X)}{\epsilon^2} < \delta$$

$\forall \mathfrak{m} > \mathfrak{m}'$, where $\mathfrak{m}' = \max\{\mathfrak{m}_1, \mathfrak{m}_2\}$. \square

Let $A^l(m)$ and $B^l(\mathfrak{m})$ denote a sequence of random matrices defined as above, corresponding to models for which $m = \min(m_1, \dots, m_{L-1})$.

Corollary 5.1.

$$\begin{aligned} B^l(m) &\xrightarrow{P} I & \forall l \in [2 \dots N] \\ A^l(m) &\xrightarrow{P} I & \forall l \in [1 \dots N - 1] \end{aligned}$$

This follows from Corr 3.1 and Thm 4.

A.2. Dynamics of Random Matrices

Consider a dynamical process, where the random matrices defined above are changed as $Q_j \rightarrow Q_j - \Delta Q_j \forall j$, and specifically from (26):

$$\Delta Q_j = \mu \left(\prod_{n=N}^{j+1} Q_n \right)^\top E_r \left(\prod_{n=j-1}^1 Q_n \right)^\top \quad (15)$$

$$E_r = \left(\prod_{n=N}^1 Q_n \right) \Sigma_{XX} - \Sigma_{YX}$$

Denoting $Q^l \rightarrow Q^l - \Delta Q^l$ and applying the product rule

$$\Delta Q^l = \sum_{j=1}^{l-1} \left(\prod_{n=l-1}^{j+1} Q_n \right) \Delta Q_j \left(\prod_{n=j-1}^1 Q_n \right) \quad (16)$$

Finally, for $B^l = \mathbf{Q}^{l\top} \mathbf{Q}^l$ and denoting $B^l \rightarrow B^l - \Delta B^l$:

$$\Delta B^l = [\Delta \mathbf{Q}^{l\top} \mathbf{Q}^l + \mathbf{Q}^{l\top} \Delta \mathbf{Q}^l] \quad (17)$$

Before proceeding to analyze ΔB^l , we note that

$$m_N \sigma_N^2 = \frac{K}{m_{N-1}} = \frac{K}{m} [1 + O\left(\frac{1}{m}\right)]$$

and therefore from Thm 3

$$\mathbb{E}[(\mathbf{Q}^{N\top}) \mathbf{Q}^N] = \left[\frac{K}{m} + O\left(\frac{1}{m}\right)\right] I \quad (18)$$

Theorem 6. For sequence $B^l(m)$ defined as above, if

$$B^l(m) \xrightarrow{p} I, \quad \text{var}[B^l(m)] = O\left(\frac{1}{m}\right)$$

then

$$\Delta B^l(m) \xrightarrow{p} 0, \quad \text{var}[\Delta B^l(m)] = O\left(\frac{1}{m}\right)$$

Proof. $B^l(m) \xrightarrow{p} I$ implies that $\forall \epsilon, \delta > 0 \exists \hat{m} \in \mathbb{N}$, such that $\forall m > \hat{m}$ and with probability larger than $1 - \delta$.

$$B^l(m) = I + e_1 \quad |e_1| < \epsilon, \quad \forall l \in [2 \dots N] \quad (19)$$

In addition, from (18) and Thms. 4,5

$$\mathbf{Q}^{N\top} \mathbf{Q}^N = \frac{K}{m} I + e_2 \quad |e_2| < \epsilon$$

We fix m and let B^l be a shorthand for $B^l(m)$. Now

$$\begin{aligned} B^{N+1} &= \mathbf{Q}_{N-1}^{\top} \mathbf{Q}^{N\top} \mathbf{Q}^N \mathbf{Q}_{N-1} \quad (20) \\ &= \frac{K}{m} \mathbf{Q}^{N-1\top} \mathbf{Q}^{N-1} + O(\epsilon) = \frac{K}{m} I + O(\epsilon) \end{aligned}$$

To evaluate ΔB^l from (17), we start from

$$\mathbf{Q}^{l\top} \Delta \mathbf{Q}^l = \sum_{j=1}^{l-1} \left(\prod_{l-1}^1 \mathbf{Q}_n \right)^\top \left(\prod_{l-1}^{j+1} \mathbf{Q}_n \right) \Delta \mathbf{Q}_j \prod_{j-1}^1 \mathbf{Q}_n$$

Simplifying t_j - the j^{th} term in the sum

$$\begin{aligned} t_j &= \mu \prod_1^{l-1} \mathbf{Q}_n^\top \prod_{l-1}^{j+1} \mathbf{Q}_n \prod_{j+1}^N \mathbf{Q}_n^\top E_r \prod_1^{j-1} \mathbf{Q}_n^\top \prod_{j-1}^1 \mathbf{Q}_n \\ &= \mu B^l (B^{j+1})^{-1} \mathbf{Q}^{N\top} E_r B^j + O(\epsilon) \end{aligned}$$

The last transition is exactly true when $B^l = I$ and $B^{j+1} = I$, as shown in Lemma 3 in App. A.3. Substituting E_r

$$\begin{aligned} t_j &= \mu B^l (B^{j+1})^{-1} \mathbf{Q}^{N\top} [\mathbf{Q}^N \Sigma_{XX} - \Sigma_{YX}] B^j + O(\epsilon) \\ &= \mu B^l (B^{j+1})^{-1} [B^{N+1} \Sigma_{XX} + \mathbf{Q}^{N\top} \Sigma_{YX}] B^j + O(\epsilon) \end{aligned} \quad 16$$

Substituting (19) and (20)

$$t_j = \mu \left[\frac{K}{m} \Sigma_{XX} + \mathbf{Q}^{N\top} \Sigma_{YX} \right] + O(\epsilon) \quad (21)$$

From (21) and Lemma 2

$$\mathbb{E}[\mathbf{Q}^{l\top} \Delta \mathbf{Q}^l] = \sum_{j=1}^{l-1} \mathbb{E}[t_j] = \mu l \frac{K}{m} I + O(\epsilon)$$

Since $\Delta \mathbf{Q}^{l\top} \mathbf{Q}^l = [\mathbf{Q}^{l\top} \Delta \mathbf{Q}^l]^\top$, it follows from (17) that

$$\mathbb{E}[\Delta B^l] = 2\mu l \frac{K}{m} I + O(\epsilon) \quad (22)$$

To conclude the proof, we need to show that $\forall \epsilon', \delta' > 0 \exists \hat{m}' \in \mathbb{N}$, such that $\forall m > \hat{m}'$

$$P(|\Delta B^l| > \epsilon') < \delta'$$

Since (22) is true with probability $(1 - \delta) \forall \epsilon, \delta$ and $\forall m > \hat{m}$, we choose ϵ and \hat{m}' such that

$$|\mathbb{E}[\Delta B^l]| < \frac{\epsilon'}{2} \quad \forall m > \hat{m}' \quad (23)$$

$$\begin{aligned} P(|\Delta B^l| > \epsilon') &\leq (1 - \delta) P\left(|\Delta B^l - \mathbb{E}(\Delta B^l)| > \frac{\epsilon'}{2}\right) \\ &< \frac{4\text{var}(\Delta B^l)}{\epsilon'^2} (1 - \delta) \end{aligned}$$

$\text{var}(\Delta B^l) = O\left(\frac{1}{m}\right)$ implies that $\exists \hat{m}'' \in \mathbb{N}, \delta > 0$, such that $\forall m > \hat{m}''$

$$\frac{4\text{var}(\Delta B^l)}{\epsilon'^2} (1 - \delta) < \delta'$$

It now follows that $\Delta B^l(m) \xrightarrow{p} 0$.

To analyze the variance, we assume that all the moments of the distribution functions used to sample Q_n are bounded. Thus, from (21), the variance of $t_j \forall j$ remains $O\left(\frac{1}{m}\right)$. Likewise, since ΔB^l is a sum of matrices, each with variance $O\left(\frac{1}{m}\right)$ thus bounding the covariance by $O\left(\frac{1}{m}\right)$, we can deduce that $\text{var}(\Delta B^l) = O\left(\frac{1}{m}\right)$. □

Theorem 7. For sequence $A^l(m)$ defined as above, if

$$A^l(m) \xrightarrow{p} I \quad \text{and} \quad \text{var}[A^l(m)] = O\left(\frac{1}{m}\right)$$

then

$$\Delta A^l(m) \xrightarrow{p} 0 \quad \text{and} \quad \text{var}[\Delta A^l(m)] = O\left(\frac{1}{m}\right)$$

The proof is mostly similar to Thm 6, though we additionally need to show the following in order to replace (18):

$$\mathbb{E}[\mathbf{Q}^0 \Sigma_{XX} \mathbf{Q}^{0\top}] = \left[\frac{q}{m} + O\left(\frac{1}{m}\right) \right] I$$

This, in turn, can be proved in similarly to Thm 3, when taking into account the initialization scheme defined in Def. 3.

Note about convergence rate. In Thm 6, convergence to 0 when $m \rightarrow \infty$ is governed by $O\left(\frac{K}{m}\right)$. In Thm 7, convergence is governed by $O\left(\frac{q}{m}\right)$.

A.3. Some Useful Lemmas

Lemma 1. Given function $G(W) = \frac{1}{2} \|UWVX - Y\|_F^2$, its derivative is the following

$$\begin{aligned} \frac{dG(W)}{dW} &= U^\top UWVX(VX)^\top - U^\top Y(VX)^\top \\ &= U^\top [UWV\Sigma_{XX} - \Sigma_{YX}]V^\top \end{aligned} \quad (24)$$

Lemma 2. Given $\mathbf{Q} = \prod_{n=N}^1 Q_n$, where $Q_n \in \mathbb{R}^{m_n \times m_{n-1}}$ denotes a random matrix whose elements are sampled iid from a distribution with mean 0 and variance σ_n^2 , $\forall i, j$.

$$\begin{aligned} \mathbb{E}[\mathbf{Q}_{ij}] &= 0 \\ \text{var}[\mathbf{Q}_{ij}] &= \frac{1}{m_N} \prod_{n=1}^N m_n \sigma_n^2 \end{aligned} \quad (25)$$

Proof. By induction on N . Clearly for $N = 1$:

$$\begin{aligned} \mathbb{E}[\mathbf{Q}_{ij}] &= \mathbb{E}[(Q_1)_{ij}] = 0 \\ \text{var}[\mathbf{Q}_{ij}] &= \text{var}[(Q_1)_{ij}] = \sigma_1^2 \end{aligned}$$

Assume that (25) holds for $N - 1$. Let $V = \prod_{n=N-1}^1 Q_n$, $U = Q_N$. It follows that

$$\begin{aligned} \mathbb{E}[\mathbf{Q}_{ij}] &= \mathbb{E}[(UV)_{ij}] = \sum_k \mathbb{E}[U_{ik}V_{kj}] \\ &= \sum_k \mathbb{E}[U_{ik}] \mathbb{E}[V_{kj}] = 0 \end{aligned}$$

where the last transition follows from the independence of U and V . In a similar manner

$$\begin{aligned} \text{var}[\mathbf{Q}_{ij}] &= \mathbb{E}[\mathbf{Q}_{ij}^2] = \mathbb{E}\left[\left(\sum_k U_{ik}V_{kj}\right)^2\right] \\ &= \mathbb{E}\left[\sum_k U_{ik}V_{kj} \sum_l U_{il}V_{lj}\right] = \sum_k \mathbb{E}[U_{ik}^2] \mathbb{E}[V_{kj}]^2 \\ &= m_{N-1} \sigma_N^2 \frac{1}{m_{N-1}} \prod_{n=1}^{N-1} m_n \cdot \sigma_n^2 \\ &= \frac{1}{m_N} \prod_{n=1}^N m_n \cdot \sigma_n^2 \end{aligned}$$

With the initialization scheme defined in Def. 3, $\text{var}(\mathbf{Q}_{ij}) = O\left(\frac{1}{m}\right)$. \square

Lemma 3. Consider matrix multiplication CD where $C \in \mathbb{R}^{k \times m}$, $D \in \mathbb{R}^{m \times k}$, $k \ll m$ and $\text{rank}(CD) = k$. Define $\Delta_1 \in \mathbb{R}^{m \times k}$, $\Delta_2 \in \mathbb{R}^{k \times m}$. Then

$$C\Delta_1 = \Delta_2\Delta_1 = I \implies CD = C\Delta_1\Delta_2D$$

Proof. Since $C = \Delta_1^+$ and $\Delta_2 = \Delta_1^+$

$$C = \Delta_1^+ \Delta_1 C = C \Delta_1 \Delta_1^+ = C \Delta_1 \Delta_2$$

\square

B. Supplementary proofs

B.1. Deep Linear networks

Here we prove Thm 1 as defined in Section 2.3.

Theorem 1. The compact matrix representation \mathbf{W} obeys the following dynamics

$$\mathbf{W}^{s+1} = \mathbf{W}^s - \mu \sum_{l=1}^L A_l^s \cdot \text{Er}^s \cdot B_l^s + O(\mu^2)$$

where the gradient scale matrices A_l^s , B_l^s are defined in (7)

$$\begin{aligned} A_l^s &\doteq \left(\prod_{j=L}^{l+1} W_j^s \right) \left(\prod_{j=L}^{l+1} W_j^s \right)^\top \in \mathbb{R}^{K \times K} \\ B_l^s &\doteq \left(\prod_{j=l-1}^1 W_j^s \right)^\top \left(\prod_{j=l-1}^1 W_j^s \right) \in \mathbb{R}^{q \times q} \end{aligned}$$

Proof. At time s , the gradient step ΔW_l^s of layer l is defined by differentiating $L(\mathbb{X})$ with respect to W_l^s . Henceforth we omit index s for clarity. First, we rewrite $L(\mathbb{X})$ as follows:

$$L(\mathbb{X}; W_l) = \frac{1}{2} \left\| \left(\prod_{j=L}^{l+1} W_j \right) W_l \left(\prod_{j=l-1}^1 W_j \right) X - Y \right\|_F^2$$

Differentiating $L(\mathbb{X}; W_l)$ to obtain the gradient $\Delta W_l = \frac{\partial L(\mathbb{X}; W_l)}{\partial W_l}$, using Lemma 1 above, we get

$$\Delta W_l = \left(\prod_{j=L}^{l+1} W_j \right)^\top [\mathbf{W} \Sigma_{XX} - \Sigma_{YX}] \left(\prod_{j=l-1}^1 W_j \right)^\top \quad (26)$$

Finally

$$\begin{aligned} \Delta \mathbf{W} &= \prod_{l=L}^1 (W_l - \mu \Delta W_l) - \prod_{l=L}^1 W_l \\ &= -\mu \sum_{l=1}^L \left(\prod_{n=L}^{l+1} W_n \right) \Delta W_l \left(\prod_{n=l-1}^1 W_n \right) + O(\mu^2) \end{aligned}$$

Substituting ΔW_l and the definition of Er in (1) into the above completes the proof. \square

B.2. Adding Non-Linear ReLU Activation

Consider the following two-layer model with ReLU activation, where only the weights of the first layer are being learned. Similarly to (5), the loss is defined as

$$L(\mathbb{X}) = \frac{1}{2} \sum_{i=1}^n \|f(\mathbf{x}_i) - \mathbf{y}_i\|^2 \quad (27)$$

$$f(\mathbf{x}_i) = \mathbf{a}^\top \cdot \sigma(W \mathbf{x}_i), \quad \mathbf{a} \in \mathbb{R}^m, \quad W \in \mathbb{R}^{m \times d}$$

m denotes the number of neurons in the hidden layer. We consider a binary classification problem with 2 classes, where $y_i = 1$ for $\mathbf{x}_i \in C_1$, and $y_i = -1$ for $\mathbf{x}_i \in C_2$. $\sigma(\cdot)$ denotes the ReLU activation function applied element-wise to vectors, where $\sigma(u) = u$ if $u \geq 0$, and 0 otherwise.

At time s , each gradient step is defined by differentiating $L(\mathbb{X})$ with respect to W . Due to the non-linear nature of the activation function $\sigma(\cdot)$, we separately³ differentiate each row of W , denoted \mathbf{w}_r where $r \in [m]$, as follows:

$$\begin{aligned} \mathbf{w}_r^{s+1} - \mathbf{w}_r^s &= -\mu \left. \frac{\partial L(\mathbb{X})}{\partial \mathbf{w}_r} \right|_{\mathbf{w}_r = \mathbf{w}_r^s} \\ &= -\mu \sum_{i=1}^n \left[\mathbf{a}^\top \cdot \sigma(W^s \mathbf{x}_i) - y_i \right] \left. \frac{\partial f(\mathbf{x}_i)}{\partial \mathbf{w}_r} \right|_{\mathbf{w}_r = \mathbf{w}_r^s} \\ &= -\mu \sum_{i=1}^n \left[\sum_{j=1}^m a_j \sigma(\mathbf{w}_j^s \cdot \mathbf{x}_i) - y_i \right] a_r \mathbf{x}_i^\top \mathbb{1}_{\mathbf{w}_r^s}(\mathbf{x}_i) \\ &= -\mu a_r \sum_{i=1}^n \mathbb{1}_{\mathbf{w}_r^s}(\mathbf{x}_i) \left[\Psi^s(\mathbf{x}_i) \cdot \mathbf{x}_i - y_i \right] \mathbf{x}_i^\top \\ &\quad \text{where } \Psi^s(\mathbf{x}_i) = \sum_{j=1}^m a_j \mathbf{w}_j^s \mathbb{1}_{\mathbf{w}_j^s}(\mathbf{x}_i) \end{aligned}$$

Above $\mathbb{1}_{\mathbf{w}_r^s}(\mathbf{x}_i)$ denotes the indicator function that equals 1 when $\mathbf{w}_r^s \cdot \mathbf{x}_i \geq 0$, and 0 otherwise.

In order to proceed, we make two assumptions:

1. The distribution of the data is symmetric where $P(\mathbf{x}_i) = P(-\mathbf{x}_i)$.
2. W and \mathbf{a} are initialized so that $\mathbf{w}_{2i}^0 = -\mathbf{w}_{2i-1}^0$ and $a_{2i} = -a_{2i-1} \quad \forall i \in [\frac{m}{2}]$.

It follows from Assumption 2 that at the beginning of training $\mathbb{1}_{\mathbf{w}_{2j}^0}(\mathbf{x}_i) + \mathbb{1}_{\mathbf{w}_{2j-1}^0}(\mathbf{x}_i) = 1, \forall \mathbf{x}_i$ such that $\mathbf{w}_{2j-1} \mathbf{x}_i \neq$

³Since the ReLU function is not everywhere differentiable, the following may be considered the definition of the update rule.

$\mathbf{w}_{2j} \mathbf{x}_i \neq 0$, and $\forall j \in [\frac{m}{2}]$. Consequently

$$\Psi^0(\mathbf{x}_i) = \sum_{j=1}^m a_j \mathbf{w}_j^0 \mathbb{1}_{\mathbf{w}_j^0}(\mathbf{x}_i) = \frac{1}{2} \sum_{j=1}^m a_j \mathbf{w}_j^0 = \frac{1}{2} \mathbf{a}^\top W^0$$

$\forall \mathbf{x}_i$ such that $\mathbf{w}_{2j-1} \mathbf{x}_i \neq \mathbf{w}_{2j} \mathbf{x}_i \neq 0$. Finally

$$\mathbf{w}_r^1 - \mathbf{w}_r^0 = -\mu a_r \left[\frac{1}{2} \mathbf{a}^\top W^0 \sum_{\substack{i=1 \\ \mathbf{w}_r^0 \cdot \mathbf{x}_i \geq 0}}^n \mathbf{x}_i \mathbf{x}_i^\top - \sum_{\substack{i=1 \\ \mathbf{w}_r^0 \cdot \mathbf{x}_i \geq 0}}^n y_i \mathbf{x}_i^\top \right]$$

Next, we note that Assumption 1 implies

$$\mathbb{E} \left[\sum_{\substack{i=1 \\ \mathbf{w} \cdot \mathbf{x}_i \geq 0}}^n \mathbf{x}_i \mathbf{x}_i^\top \right] = \frac{1}{2} \mathbb{E} \left[\sum_{i=1}^n \mathbf{x}_i \mathbf{x}_i^\top \right] = \frac{1}{2} \mathbb{E} [\Sigma_{XX}]$$

for any vector \mathbf{w} . Thus, if the sample-size n is large enough, at the beginning of training we expect to see

$$\mathbf{w}_r^{s+1} - \mathbf{w}_r^s \approx -\mu \frac{a_r}{2} [\mathbf{a}^\top W^s \Sigma_{XX} - \tilde{\mathbf{m}}_r^s] \quad \forall r$$

where row vector $\tilde{\mathbf{m}}_r^s$ denotes the vector difference between the centroids of classes C_1 and C_2 , computed in the half-space defined by $\mathbf{w}_r^s \cdot \mathbf{x} \geq 0$. Finally (for small s)

$$W^{s+1} - W^s \approx -\mu \frac{1}{2} \left[(\mathbf{a} \mathbf{a}^\top) W^s \Sigma_{XX} - \tilde{M}^s \right]$$

where \tilde{M}^s denotes the matrix whose r -th row is $a_r \tilde{\mathbf{m}}_r^s$.

C. Additional Empirical Results

C.1. Weight Initialization

We evaluate empirically the weight initialization scheme from Def. 3. When compared to Glorot uniform initialization (Glorot & Bengio, 2010), the only difference between the two schemes lies in how the first and last layers are scaled. Thus, in order to highlight the difference between the methods, we analyze a fully connected linear network with a single hidden layer, whose dimension (the number of hidden neurons) is much larger than the input and output dimensions. We trained $N=10$ such networks on a binary classification problem, once with the initialization suggested in Def. 3, and again with Glorot uniform initialization. While both initialization schemes achieve the same final accuracy upon convergence, our proposed method converges faster on both train and test datasets (see Fig. 12).

C.2. Classification on the Frequency Dataset

We trained $N=100$ st-VGG networks on the frequency dataset (see App. D.3). Since the data lies in \mathbb{R}^2 , we can visualize it and the corresponding network's inter-class boundary

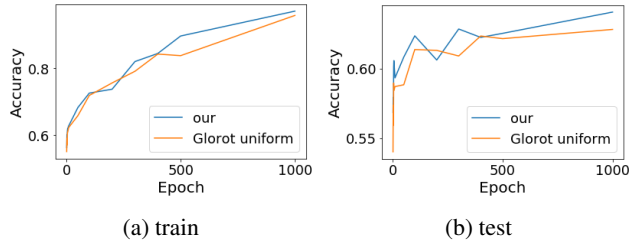


Figure 12. Learning curves of a fully connected linear network with one hidden layer, trained on the dogs and cats dataset, and initialized by Glorot uniform (orange) and the initialization proposed in Def. 3 (blue).

at each epoch as shown in Fig. 13, which tracks the decision function of one st-VGG network through learning. Each point represents a training example (yellow for one class and purple for the other). The background color represents the classification that the network predicts for points in that region. The presented epochs (from left to right): 1, 100, 1000, 10000. We can see that the decision function incorporates low frequencies at the beginning of the learning, adding the higher frequencies only later on. The same qualitative results are achieved with other instances of st-VGG as well. We note that while the decision functions are very similar in the region where the training data is, at points outside of the data they differ drastically across networks.

D. Methodology

The results reported in Section 6.1 represent the mean performance of 100 st-VGG and linear st-VGG networks, trained on the small mammals dataset. The results reported in Section 6.2 represent the mean performance of 10 2-layers fully connected linear networks trained over the cats and dogs dataset. The results in Fig. 11 represent the mean performance of 100 st-VGG network trained on the small mammals dataset. In every experimental setup the network’s hyper-parameters were coarsely grid-searched to achieve good performance over the validation set, for fair comparison. Other hyper-parameters exhibit similar results.

D.1. Generalization Gap

In Section 6.1 we discuss the evaluation of networks on datasets with amplified principal components. Examples of these images are shown in Fig. 14: the top row shows examples of the original images, the middle row shows what happens to each image when its 1.5% most significant principal components are amplified, and the bottom row shows what happens when its 1.5% least significant principal components are amplified. Amplification was done by a factor of 10, which is significantly smaller than the ratio between the values of the first and last principal components of the data. After amplification, all the images were re-normalized

to have 0 mean and std 1 in every channel as customary.

D.2. Architectures

st-VGG. A stripped version of VGG which we used in many of the experiments. It is a convolutional neural network, containing 8 convolutional layers with 32, 32, 64, 64, 128, 128, 256, 256 filters respectively. The first 6 layers have filters of size 3×3 , and the last 2 layers have filters of size 2×2 . Every other layer is followed by a 2×2 max-pooling layer and a 0.25 dropout layer. After the convolutional layers, the units are flattened, and there is a fully-connected layer with 512 units followed by 0.5 dropout. The batch size we used was 100. The output layer is a fully-connected layer with output units matching the number of classes in the dataset, followed by a softmax layer. We trained the network using the SGD optimizer, with cross-entropy loss. When training st-VGG, we used a learning rate of 0.05.

Linear st-VGG. A linear version of the st-VGG network. In linear st-VGG, we change the activation function to the identity function, and replace max-pooling by average pooling with a similar stride.

Linear fully connected network. An L -layered fully connected network. Each layer contains 1024 weights, initialized with Glorot uniform initialization. 0.5 dropout is used before the output layer. Networks are trained with an SGD optimizer, without momentum or L_2 regularization.

D.3. Datasets

In all the experiments and all the datasets, the data was always normalized to have 0 mean and std 1, in each channel separately.

Small Mammals. The small-mammals dataset used in our experiments is the relevant super-class of the CIFAR-100 dataset. It contains 2500 train images divided into 5 classes equally, and 500 test images. Each image is of size $32 \times 32 \times 3$. This dataset was chosen due to its small size.

Cats and Dogs. The cats and dogs dataset is a subset of CIFAR-10. It uses only the 2 relevant classes, to create a binary problem. Each image is of size $32 \times 32 \times 3$. The dataset is divided to 20000 train images (10000 per class) and 2000 test images (1000 per class). This dataset is used when a binary problem is required.

ImageNet-20. The ImageNet-20 dataset is a subset of ImageNet containing 20 classes. This data resembles ImageNet in terms of image resolution and data variability, but contains a smaller number of examples in order to reduce computation time. The dataset contains 26000 train images (1300 per class) and 1000 test images (50 per class). The choice of the 20 classes was arbitrary, and contained the following classes: boa constrictor, jellyfish, American lobster,

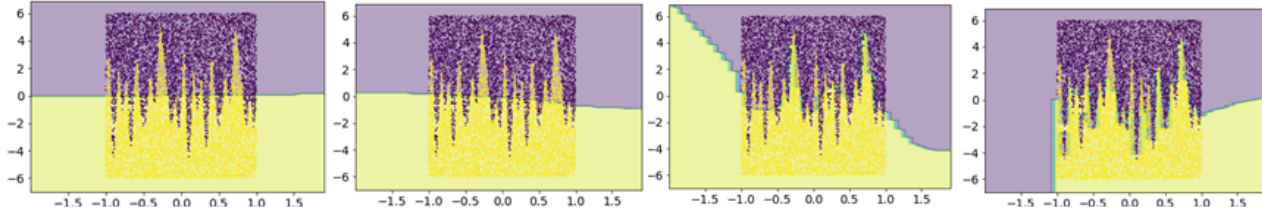


Figure 13. Visualization the separator learned by st-VGG when trained on the frequency dataset, as captured in advancing epochs.

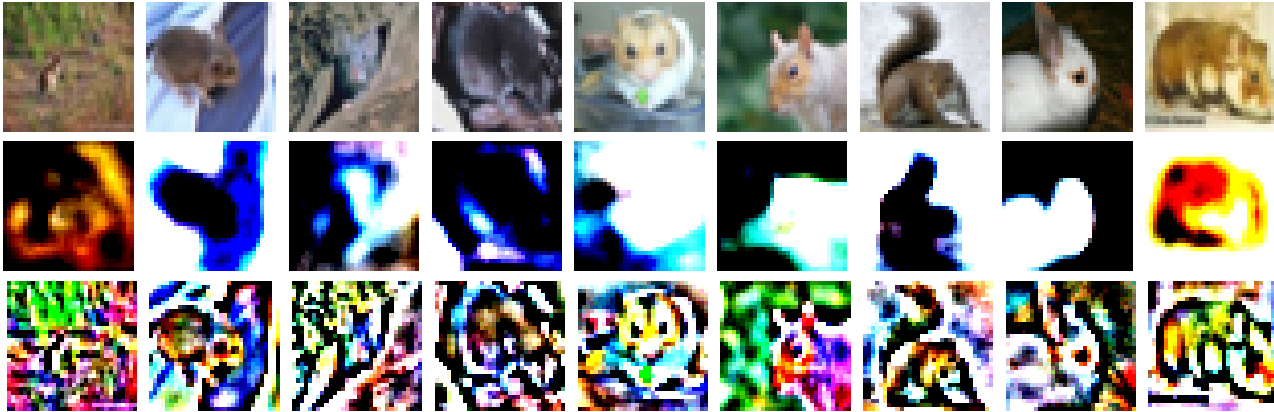


Figure 14. Visualization of the small mammals dataset, with amplification of 1.5% of its principal components by a factor of 10. Top: original data; middle: data amplified along the first principal components; bottom: data amplified along the last principal components

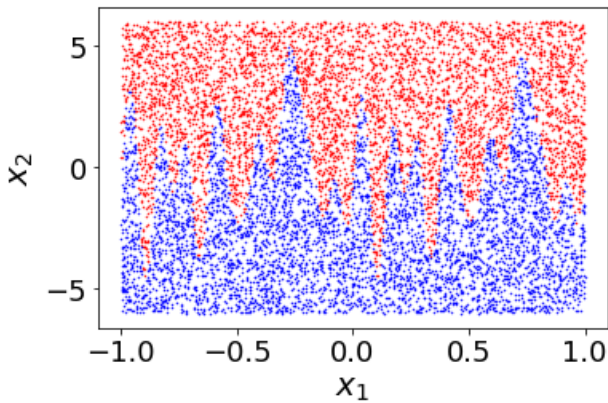


Figure 15. Visualization of the classification dataset used to extend Rahaman et al. (2019) to a classification framework.

little blue heron, Shih-Tzu, scotch terrier, Chesapeake Bay retriever, komondor, snow leopard, tiger, long-horned beetle, warthog, cab, holster, remote control, toilet seat, pretzel, fig, burrito and toilet tissue.

Frequency dataset A binary 2D dataset, used in Section 5, to examine the effects of spectral bias in classification. The data is define by the mapping $\lambda : [-1, 1] \rightarrow \mathbb{R}$ given in (11)

by

$$\lambda(z) = \sum_{i=1}^m \sin(2\pi\kappa_i z + \varphi_i) := \sum_{i=1}^m \text{freq}_i(z)$$

with frequencies $\kappa = (\kappa_1, \kappa_2, \dots, \kappa_m)$ and corresponding phases $\phi = (\varphi_1, \varphi_2, \dots, \varphi_m)$. The classification rule is defined by $\lambda(z) \leq 0$.

In our experiments, we chose $m = 10$, with frequencies $\kappa_1 = 0, \kappa_2 = 1, \kappa_3 = 2, \dots, \kappa_{10} = 9$. Other choices of m yielded similar qualitative results. The phases were chosen randomly between 0 and 2π , and were set to be: $\varphi_1 = 0, \varphi_2 = 3.46, \varphi_3 = 5.08, \varphi_4 = 0.45, \varphi_5 = 2.10, \varphi_6 = 1.4, \varphi_7 = 5.36, \varphi_8 = 0.85, \varphi_9 = 5.9, \varphi_{10} = 5.16$. As the first frequency is $\kappa_1 = 0$, the choice of φ_0 does not matter, and is set to 0. The dataset contained 10000 training points, and 1000 test points, all uniformly distributed in the first dimension between -1 and 1 and in the second dimension between -2π and 2π . The labels were set to be either 0 or 1, in order to achieve perfect separation with the classification rule $\lambda(z)$ (see visualization in Fig. 15).

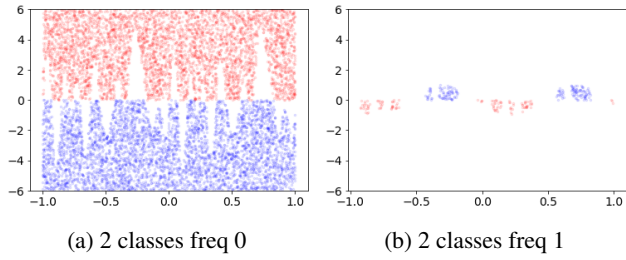


Figure 16. Visualization of the *critical frequency*, showing all the points in the 2D-frequency dataset with *critical frequency* of (a) 0, and (b) 1.

D.4. Critical Frequency

In Section 5.2 we defined the *critical frequency* of an example. In Fig. 16, we see a visualization of this measure on the frequency dataset. In Fig. 16a, we plot all the points with *critical frequency* of 0. In Fig. 16b, we can see all the points with *critical frequency* of 1.